



UMEÅ UNIVERSITY

# Digital holography and image processing methods for applications in biophysics

Hanqing Zhang

Doctoral Thesis  
Department of Physics  
Umeå University  
Umeå 2018

This work is protected by the Swedish Copyright Legislation (Act 1960:729)  
Dissertation for PhD  
ISBN: 978-91-7601-915-3  
Electronic version available at: <http://umu.diva-portal.org/>  
Printed by: UmU Print Service  
Umeå, Sweden 2018

*Dreams and dedication are a powerful combination.*

*William Longgood*



# Table of Contents

<b>Abstract.....</b>	<b>iii</b>
<b>Abbreviations.....</b>	<b>iv</b>
<b>Sammanfattning .....</b>	<b>v</b>
<b>List of Publications .....</b>	<b>vi</b>
<b>1. Introduction.....</b>	<b>1</b>
1.1    Background .....	1
1.2    Imaging techniques.....	1
1.3    Aim of the thesis.....	4
1.4    Outline of the thesis .....	5
<b>2. Digital Holographic Microscopy.....</b>	<b>6</b>
2.1    From waves to holograms.....	6
2.2    Scalar diffraction theory .....	8
2.3    Hologram construction and reconstruction.....	10
2.4    Experimental setup and sample preparation.....	11
2.5    Synthetic data generation .....	12
<b>3. Diffraction Pattern Detection.....</b>	<b>14</b>
3.1    Features in the hologram.....	14
3.2    Circle detection using isosceles triangles sampling.....	15
3.3    Refinement of the central position of an object.....	19
<b>4. Object Tracking in 3D.....</b>	<b>20</b>
4.1    Image tracking framework .....	20
4.2    Pre-processing.....	20
4.3    Particle center localization.....	21
4.4    Tracking.....	21
4.5    Numerical intensity reconstruction .....	22
4.6    Fluidic flow profiling.....	24
<b>5. Multiple-Wavelength Approach .....</b>	<b>27</b>
5.1    Defining the object plane in DHM .....	27
5.2    Multi-wavelength Gerchberg-Saxton algorithm .....	27
5.3    Phase reconstruction .....	30
5.4    Object plane position detection .....	32
5.5    Tracking of cells using multiple-wavelength in-line DHM .....	35
<b>6. Image Segmentation and Applications .....</b>	<b>36</b>
6.1    Overview of image segmentation methods .....	36
6.2    Level set method for time-varying objects .....	37
6.3    Image segmentation of <i>E. coli</i> cells .....	39
6.4    Estimating the drag force on <i>E. coli</i> cells .....	40
6.5    Segmentation of growing bacteria and backbone extraction .....	41
<b>7. Development of Software Tools.....</b>	<b>43</b>
7.1    UmUTracker.....	43

7.2	Capsule Cell Tracker .....	43
7.3	DSeg.....	43
<b>8.</b>	<b>Concluding Remarks and Outlook.....</b>	<b>44</b>
8.1	Future Applications .....	45
	<b>Summary of papers .....</b>	<b>46</b>
	<b>Acknowledgement.....</b>	<b>51</b>
	<b>References .....</b>	<b>52</b>

# **Abstract**

Understanding dynamic mechanisms, morphology and behavior of bacteria are important to develop new therapeutics to cure diseases. For example, bacterial adhesion mechanisms are prerequisites for initiation of infections and for several bacterial strains this adhesion process is mediated by adhesive surface organelles, also known as fimbriae. *Escherichia coli* (*E. coli*) is a bacterium expressing fimbriae of which pathogenic strains can cause severe diseases in fluidic environments such as the urinary tract and intestine. To better understand how *E. coli* cells attach and remain attached to surfaces when exposed to a fluid flow using their fimbriae, experiments using microfluidic channels are important; and to assess quantitative information of the adhesion process and cellular information of morphology, location and orientation, the imaging capability of the experimental technique is vital.

In-line digital holographic microscopy (DHM) is a powerful imaging technique that can be realized around a conventional light microscope. It is a non-invasive technique without the need of staining or sectioning of the sample to be observed *in vitro*. DHM provides holograms containing three-dimensional (3D) intensity and phase information of cells under study with high temporal and spatial resolution. By applying image processing algorithms to the holograms, quantitative measurements can provide information of position, shape, orientation, optical thickness of the cell, as well as dynamic cell properties such as speed, growing rate, etc.

In this thesis, we aim to improve the DHM technique and develop image processing methods to track and assess cellular properties in microfluidic channels to shed light on bacterial adhesion and cell morphology. To achieve this, we implemented a DHM technique and developed image processing algorithms to provide for a robust and quantitative analysis of holograms. We improved the cell detection accuracy and efficiency in DHM holograms by developing an algorithm for detection of cell diffraction patterns. To improve the 3D detection accuracy using in-line digital holography, we developed a novel iterative algorithm that use multiple-wavelengths. We verified our algorithms using synthetic, colloidal and cell data and applied the algorithms for detecting, tracking and analysis. We demonstrated the performance when tracking bacteria with sub-micrometer accuracy and kHz temporal resolution, as well as how DHM can be used to profile a microfluidic flow using a large number of colloidal particles. We also demonstrated how the results of cell shape analysis based on image segmentation can be used to estimate the hydrodynamic force on tethered capsule-shaped cells in micro-fluidic flows near a surface.

# Abbreviations

3D	Three-Dimensional
AFM	Atomic Force Microscopy
CCD	Charge-Coupled Device
CoM	Center-of-Mass
CFD	Computational Fluid Dynamics
CPU	Central Processing Unit
DDA	Discrete Dipole Approximation
DHM	Digital Holographic Microscopy
DIC	Differential Interference Contrast
DNN	Deep Neural Networks
DoG	Difference of Guassians
GUI	Graphical User Interface
<i>E. coli</i>	<i>Escherichia Coli</i>
EM	Electron Microscopy
FPGA	Field Programmable Gate Array
GPU	Graphics Processing Unit
ITs	Isosceles Triangles
PBS	Phosphate Buffered Saline
PDMS	Polydimethylsiloxane
PS	Polystyrene
QI	Quadrant Interpolation
SD	Standard Deviation
<i>S. coelicolor</i>	<i>Streptomyces Coelicolor</i>
RBC	Red Blood Cell
ROI	Region-Of-Interest
RGB	Red Green Blue
TSB	Tryptic Soy Broth
LED	Light Emitting Diode
OPL	Optical Path Length

# Sammanfattning

Att förstå dynamiska mekanismer och beteenden hos bakterier är viktiga för att utveckla nya metoder för att bota sjukdomar. Till exempel så är bakteriers förmåga att fästa mot ytor en förutsättning för att skapa infektionssjukdomar, och flera bakteriestammar uttrycker för detta ändamål ytorganeller, så kallade fimbrier, vilka binder mot ytreceptorer. *Escherichia coli* (*E. coli*) är en vanlig bakterie som uttrycker fimbrier, och många av dessa patogena stammar kan orsaka allvarliga sjukdomar i miljöer som urinvägarna och tarmarna. För att bättre förstå hur *E. coli* bakterier fäster mot ytor i sådana miljöer, där även höga vätskeflöden sker, är experiment i mikroflödeskanner viktiga; och för att samla in kvantitativ information om vidhäftningsprocessen och cellernas morfologi, lokalisering och orientering är avbildningstekniken viktig.

Så kallad In-line digital holografisk mikroskop (DHM) är en kraftfull avbildningsteknik som kan byggas upp runt ett vanligt mikroskop. Det är en icke-invasiv teknik utan behov av färgning eller snittning av provet som skall observeras. DHM tillhandahåller hologram som innehåller tredimensionell (3D) intensitet och fasinformation av celler som studeras. Genom att använda bildbehandlingsalgoritmer för att analysera hologrammen kan kvantitativa mätningar ge information om cellens position, form, orientering, optisk tjocklek, såväl som dynamiska cellegenskaper såsom hastighet, och växthastighet etc.

I denna avhandling visar jag hur man kan förbättra DHM-tekniken och utveckla bildbehandlingsalgoritmer för att mäta cellens position och cellens egenskaper i mikroflödeskanner för att förstå bakteriers vidhäftningsförmåga. För att genomföra detta utvecklar vi DHM-tekniken och bildbehandlingsalgoritmer för att möjliggöra en robust och kvantitativ analys av hologram. Vi förbättrade celldetekteringsnoggrannheten och effektiviteten i DHM-hologram genom att utveckla en algoritm för detektering av cellens diffractionsmönster. För att förbättra mätning av cellens 3D-position utvecklar vi en ny iterativ algoritm för DHM där flera våglängder används. Vi verifierar våra algoritmer med hjälp av syntetisk data, mikropartiklar och celler samt tillämpar algoritmerna för detektering, spårning och analys. Vi visar även hur man kan lokalisera bakterier med sub-mikrometernoggrannhet med kHz upplösning. Dessutom visar vi hur DHM kan användas för att mäta flödesprofilen i en mikroflödeskanal genom att följa ett stort antal mikropartiklar. Vi visar också hur bildsegmentering kan användas för att uppskatta den hydrodynamiska kraften på bundna kapselformade celler i vätskeflöden nära en yta.

# List of Publications

This thesis is based on the following publications:

- I. A fast and robust circle detection method using isosceles triangles sampling  
**H. Zhang**, K. Wiklund, and M. Andersson. *Pattern Recognition* 54: 218–228 (2016).
- II. Detecting bacterial surface organelles on single cells using optical tweezers  
J. Zakrisson, B. Singh, P. Svenmarker, K. Wiklund, **H. Zhang**, S. Hakobyan, M. Ramstedt, and M. Andersson. *Langmuir* 32 (18), 4521-4529 (2016)
- III. Refining particle positions using circular symmetry  
A. Rodriguez, **H. Zhang**, K. Wiklund, T. Brodin, J. Klaminder, P.L. Andersson, and M. Andersson. *PLoS One* 12(4): e0175015 (2017).
- IV. UmUTracker: A versatile MATLAB program for automated particle tracking of 2D light microscopy or 3D digital holography data  
**H. Zhang**, T. Stangner, K. Wiklund, A. Rodriguez, and M. Andersson. *Computer Physics Communication* 219: 390–399 (2017).
- V. Step-by-step guide to reduce spatial coherence of laser light using a rotating ground glass diffuser  
T. Stangner, **H. Zhang**, T. Dahlberg, K. Wiklund, and M. Andersson. *Applied Optics* 56: 5427 (2017).
- VI. 3D printed water-soluble scaffolds for rapid production of PDMS microfluidic flow chambers  
T. Dahlberg, T. Stangner, **H. Zhang**, K. Wiklund, P. Lundberg, L. Edman, and M. Andersson. *Scientific Reports* 8(1):3372 (2018).
- VII. A drag force interpolation model for capsule-shaped cells in fluid flows near a surface.  
K. Wiklund, **H. Zhang**, T. Stangner, B. Singh, E. Bullitt, and M. Andersson. *Microbiology* 164: 483–494 (2018).

- VIII. Object plane detection and phase retrieval from single-shot holograms using multi-wavelength in-line holography  
**H. Zhang**, T. Stangner, K. Wiklund and M. Andersson. Submitted to Applied Optics (2018).
- IX. DSeg : A dynamic image segmentation program to extract backbone patterns for filamentous bacteria and hyphae structures  
**H. Zhang**, N. Söderholm, L. Sandblad, K. Wiklund and M. Andersson. In manuscript (2018).

*All papers have been reprinted with permission of the publishers.*

Other publications by the author, not included in the thesis:

- X. ToxId: an efficient algorithm to solve occlusions when tracking multiple animals  
A. Rodriguez, **H. Zhang**, J. Klaminder, T. Brodin, and M. Andersson. Scientific Reports 7: 14774 (2017)
- XI. ToxTrac: a fast and robust software for tracking organisms  
A Rodriguez, **H. Zhang**, J Klaminder, T Brodin, P. L. Andersson, M. Andersson. Methods in Ecology and Evolution 9(3), 460-464 (2018)



# 1. Introduction

## 1.1 Background

The increasing number of multidrug-resistant bacterial infections is one of the most important threats to public health [1]. To solve this problem, we need to continuously develop new effective methods to stop pathogenic bacteria from causing infections. However, to reach this goal, we need better understanding of the bacterial infection process. Therefore, understanding the dynamic mechanisms, morphology and behavior of bacteria are important to development new therapeutics.

Since bacterial adhesion is the initial step in colonization and infection, understanding the adhesion mechanisms are important [2]. Many bacterial strains including *E. coli* use adhesive organelles, also known as fimbriae, to initiate and maintain adhesion to host surfaces [2]. For example, uropathogenic and enterotoxigenic *E. coli* are fimbriae expressing pathogenic strains that cause diseases in fluidic environments such as the urinary tract and intestine [3]. It has been shown that fimbriae expressed by these strains are flexible polymers with delicate biomechanical properties that can improve adhesion to a receptor [4]–[10]. Thus, to understand how pathogenic *E. coli* strains can sustain fluid flows *in vivo*, experiments mimicking these conditions are important.

Experiments and analysis of numerous micrometer sized objects in a micrometer sized fluid flow channel require not only sophisticated imaging capabilities but also image processing algorithms to process, detect and track the cells under investigation. However, it is a challenge in multidisciplinary research to develop technologies to obtain accurate and detailed cellular-level data of cell morphology, location and orientation.

## 1.2 Imaging techniques

To achieve accurate and high throughput measurements of living cells in a microfluidic channel, a suitable microscopy technology that meet our demands is needed. Development of the microscope to image small objects can be traced back to the invention of a lens from a polished crystal. However, during the recent decades we have witnessed how high-quality detectors, cutting-edge illumination systems and computer-based techniques have improved the quality of the assessed data and helped us advance our understanding of the dynamic behavior of cells and their structures. Computational techniques are central in this improvement, where algorithms are developed to reconstruct structures and solve imaging problems. In addition, general image analysis tools have been developed to allow researchers to apply image processing algorithms in a simple manner.

Nowadays, state-of-the-art microscopy systems are equipped with different computational techniques depending on a diverse range of applications in practice. Depending on the sample type, size, and optical property as well as the resolution of the microscopy, the advantages and disadvantages of some general techniques are discussed here. For example, in structural biology, advanced electron microscopy (EM) based

technique have obtained near-atomic-resolution ( $<4$  Å) from reconstructions, e.g., by using cryo-EM data [11]. However, EM imaging does not allow for imaging of living cells. Atomic force microscope (AFM) can be applied to capture nanometer-resolution images of living biological samples in liquids and they can provide information of small structures [13]. However, the sampling process using mechanical probes in the AFM is time-consuming, requiring seconds to minutes to complete the scan and therefore the temporal resolution is low. Besides, since the properties measured by the AFM is an invasive process and dependent on the geometric characteristics of the probe tip, the artifact from contact may lead to error in quantitative measurement of the cell at molecule-level.

Molecule-level resolution can also be achieved by using optical techniques such as fluorescence microscopy [14]. This technique benefits from single particle analysis routines [15] and super-resolution microscopy [16] to overcome the diffraction limit. Although staining cells can increase the contrast and help us to observe structure better, the by-product of staining may change the properties of living cells. To visualize transparent and tiny objects without labelling, phase contrast imaging transform phase variation to amplitude to distinguish cellular and sub-cellular morphologies for biological samples with low light absorption property [17]–[19]. Similarly, the classic differential interference contrast (DIC) microscope convert phase gradients into intensity differences [20]. This interference pattern, however, is used only for qualitative phase imaging because the relationship between the DIC images and the optical path length (OPL) of the object is not linearly related [21]. To study a cell and obtain a quantitative measurement, quantitative phase microscopy (QPM) is used to dynamically measure living cells and optically transparent specimens in a quantitative, non-invasive and label-free manner [22]–[24]. By convention, there are a variety of names to describe this technique [25]. In this thesis, we describe it as digital holographic microscopy (DHM).

Holographic microscopy (light or electron) was first invented by Dennis Gabor in 1948 [26] and developed to its digital form by Goodman and Lawrence in [27]. DHM has received attention for having extended depth of focus and quantitative measurement of the optical properties of cells. A DHM setup is typically designed using an inverted bright field microscope and can record a hologram that contains all the information necessary to reconstruct the amplitude and phase of a propagating light field at different spatial positions. This allows for accurate 3D object positioning and for assessment of different parameters of a cell, such as its thickness, volume, and refractive index. In general, DHM not only shares many advantages of other light microscopy systems but also has unique features [24], [28]. First, it is a non-destructive and non-invasive method since the sample in DHM does not need any staining or sectioning to observe objects *in vitro*. Second, the construction of DHM can be compact and simple. It can be implemented directly into a conventional microscopy by sharing the optical path in the system. Besides, it allows for multimodal microscopy [29], [30] that is combined with existing systems, e.g., optical tweezers [31], Raman spectroscopy [32] or fluorescence microscopy [33]. Third, the 3D information of the sample is acquired from single hologram. Unlike the 3D information

generated by confocal microscopy [34] or fluorescence microscopy, it does not require mechanical scanning of the sample at different position in depth which allows for kHz recording of holograms. Thus, cell dynamics can be captured at high temporal resolution. Fourth, the OPL of the sample under observation is related to the index of refraction, making DHM suitable for study of cell morphology.

However, there are two major limitations in this technique. The first limitation is the accuracy and efficiency of the numerical reconstruction. The accuracy is limited not only by the wavelength of illumination used in the system but also by the parameters in the numerical reconstruction. For example, if a low-resolution hologram or a small template cut from the hologram is used as input for the numerical reconstruction procedure, the resultant 3D information will contain large error due to the quantized pixel values and template size. The numerical reconstruction is a computational demanding process so that implementation of algorithms and performance of computers are important to reach desired accuracy. To overcome this difficulty, fast processing using parallel computing, e.g., based on CPU [35], GPU [36] and field-programmable gate array (FPGA) implementation [37] are suggested. Moreover, the algorithm efficiency can be optimized in some special cases, e.g., algorithm designed only for extracting mean particle size [38] or positioning of spherical particles [39].

The second limitation is the loss of the phase of the light when the hologram is sampled on a detector, i.e., CMOS or CCD camera. To elaborate this issue, we consider an optically transparent object which provides a significant optical phase delay. This phase delay, caused by light transmitted and scattered off from an object that interferes with references light, results in a fringe pattern. The separation between scattered light of the object and the reference light can be achieved using spatial modulation. There are two spatial modulation schemes: in-line and off-axis. For in-line DHM, weakly scattered light from the object overlaps directly with the non-scattered reference light [40]. The scattered light is reconstructed by back-propagating light from hologram to the object position. In this process, the detector obtains the initial amplitude of a wave at the hologram. However, the initial phase values of wave are lost, leading to a so-called "twin image" problem [41] which add noise to the reconstruction results. To avoid this problem, various off-axis DHM schemes have been developed to acquire phase information based on a Mach-Zehnder configuration. With this configuration, the reference light is slightly tilted with respect to the object light, which gives a well-defined carrier spatial frequency [25]. By using this carrier frequency, the "twin image" information can be easily removed and the phase can be retrieval directly from spatial frequency domain. However, this approach solves the phase information at a cost of spatial resolution in the lateral plane according to the way it processes the space-bandwidth-product [42].

Recently, solutions to the "twin image" problems for in-line DHM have been proposed by [43]. To resolve the twin image problem, Gerchberg-Saxton iterative methods [44] with physical constraints have proved to have better accuracy in reconstructing phase information than those using a non-iterative approach [45]. The solution show that the in-line DHM has the potential of removing the "twin image" by

numerical methods and simultaneously acquire better spatial resolution than off-axis DHM.

Based on the solution using iterative phase retrieval, methods have been developed that samples holograms at different heights [46]–[48]; angles [49], [50]; or wavelengths [51]–[53] to solve the twin image problem for accurate phase reconstruction. All these methods solve the twin image problem for accurate phase retrieval. However, holograms acquired at different height often require mechanical scanning with a sample stage, increasing the complexity of experimental procedure [46], [48]. In addition, acquiring several images at different height often requires the object to be immobilized. To allow for studies of objects in motion, dual-plane digital holography with multiplexed volume holographic gratings can produce single-shot holograms from different heights [47]. Besides, by using holograms recorded at different heights, angles and wavelengths all together, a propagation phasor approach can be applied to reduce the number of raw measurements [50]. However, these approaches can retrieve the phase at a cost of increased complexity of the setup and alignment procedure. On the other hand, some multiple wavelength methods use relatively simple compact setups. In this case, the phase can be retrieved either by using different wavelengths that match the channels of a red-green-blue (RGB) camera [49], [54], [55], or tunable lasers can be used to acquire holograms at approximately ten to twenty different wavelengths, however at the cost of computational efficiency when processing the data [51], [52]. Thus, there is still room for developing the DHM system to achieve high framerate in recording holograms and design efficient algorithms to acquire both the intensity and phase information with high accuracy.

In summary, modern quantitative microscopy systems need to produce high quality images with powerful image processing and reconstruction algorithms that allow us to obtain reliable, high throughput analysis and reproducible results to study cells in fluidic flow. The information of a cell measured by the system should contain three-dimensional location at high spatial and temporal resolution, and shape property with low noise. The experimental design should be flexible to combine with existing microscope setup or system without introducing complicated alignment or experimental procedure to study objects in motion. The last feature is receiving a lot of interests in recent years and becoming important for modern multimodal microscopy system [29]–[33], [56], [57] that allows for registration of quantitative object properties from different techniques, and for automated detection and recognition of cells.

### **1.3 Aim of the thesis**

The work in this thesis has been aimed to develop image processing methods and apply these methods to digital images and holograms to study bacterial cells in microfluidic channels. In addition, we aimed to develop general-purpose image processing algorithms and improve the in-line DHM technique to achieve better accuracy when performing numerical reconstruction of the intensity and the phase. In pursuit of this aim, we developed a multiple wavelengths in-line digital holographic microscopy system using a

series of novel algorithms to: detect object positions; track object trajectories; retrieved the phase and analyze optical and morphological properties of objects. Furthermore, we aim to apply our DHM technique for tracking the position of *E. coli* cells of various shapes in a fluidic channel. These new approaches can thus be used to shed light on the bacterial adhesion mechanism.

#### **1.4 Outline of the thesis**

The thesis is organized into eight chapters. The second chapter introduces the fundamental theory of digital holography and the experimental setups. In the third chapter, a novel image processing method is presented for detecting diffraction pattern in holograms acquired under noisy conditions. In the fourth chapter, the realization of a 3D particle tracking system based on DHM is presented. In the fifth chapter, a novel object plane detection and phase retrieval method is presented to acquire the object position with various shapes and refractive indexes. In the sixth chapter, cell morphology analysis using our image segmentation methods is presented and how this can be used to estimate the drag force of a cell in a fluidic channel. In the seventh chapter, software tools are presented for applications in particle tracking, force estimation and morphology analysis. In the eighth chapter, concluding remarks are presented, and we discuss the potential future development of our technique for studying bacterial adhesion.

## 2. Digital Holographic Microscopy

### 2.1 From waves to holograms

To make the best effort in our multidisciplinary research to study microscopic cells in fluidic flows we combine image processing, physics and biology together with the DHM technique. This can provide us with high throughput data using an automatic, fast and robust approach. To better understand this approach, the key elements in DHM is introduced in this chapter, that is: scalar diffraction theory; numerical reconstruction; the experimental setup; and generation of synthetic data for biological applications.

In the in-line version of digital holographic microscopy, as illustrated in Figure 2.1, we start by describing how a hologram is created. A micrometer sized semi-transparent object, e.g., a cell, is illuminated by a partially coherent light source. Light that hits the object will be both scattered and transmitted by the object, and this light interferes later with non-scattered light. The hologram is created at the detector by interference of a reference wave with diffracting waves from the object. This hologram contains 3D spatial information of wave amplitude and phase related to the interaction between light and the investigated object. This information can be used to locate object positions, extract morphological properties such as shape and orientation, optical properties such as optical thickness, refractive index, as well as dynamic cell properties such as the speed, motility, growing rate, etc. The method to extract the information for the object is often related to a process named numerical reconstruction. This reconstruction process is used to simulate light propagation from the hologram. Therefore, it is important to describe light propagation and the hologram in a systematic way.

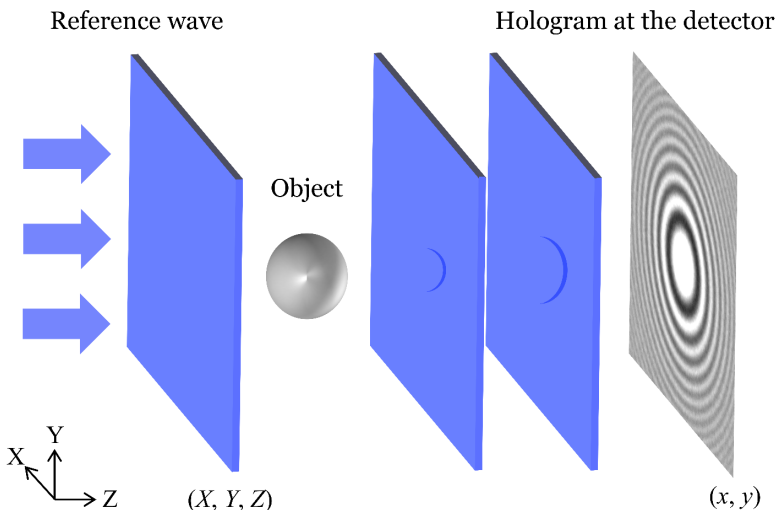


**Figure 2.1.** Schematic of in-line digital holography. An object is illuminated with a reference wave with a plane wavefront from the left. At the far right a hologram is formed by interference of waves diffracted by the object and non-diffracted waves.

To describe the waves and the hologram at the detector, we define two coordinate systems (Figure 2.1). One is defined by using a Cartesian coordinate ( $X$ ,  $Y$ ,  $Z$ ) to describe the reference wave and the diffracting waves from the object. In this coordinate system, the  $Z$ -axis is in the direction of light propagation. The other one is a 2D-system to describe a hologram in the  $xy$ -plane. Besides, we denote the  $-Z$  direction as the axial direction in which the distance  $z$  is defined from the hologram to a parallel lateral plane. Note that in a perfectly aligned system, the  $xy$ -plane is parallel to the  $XY$ -plane.

By using the coordinate systems defined above, light propagates through the object and hits the detector at position  $Z_D$  in the  $Z$  direction and is recorded as a 2D image in the lateral  $xy$ -plane. In this process, we can model the wave propagation based on scalar diffraction theory [58], [59] (see Section 2.3 for more details) and the intensity in the hologram is thus described by the superposition of the reference and diffracting waves from the object as,

$$\begin{aligned} H(x, y, 0) &= |\tilde{U}_R(X, Y, Z_D) + \tilde{U}_O(X, Y, Z_D)|^2 \\ &= |\tilde{U}_R(X, Y, Z_D)|^2 + |\tilde{U}_O(X, Y, Z_D)|^2 \\ &\quad + \tilde{U}_R^*(X, Y, Z_D)\tilde{U}_O(X, Y, Z_D) + \tilde{U}_R(X, Y, Z_D)\tilde{U}_O^*(X, Y, Z_D), \end{aligned} \quad (2.1)$$

where  $\tilde{U}_R$  represents the non-scattered reference wave and  $\tilde{U}_O$  is the scattered wave from the object,  $*$  is the complex conjugate and  $H(x, y, 0)$  represent the hologram located in 3D space with its axial distance  $z = 0$  by default. Note that the reference intensity (the first term in Equation 2.1 is a constant background, and the object intensity (the second term in Equation 2.1 is small compared to the intensity of the reference wave and thus neglected. The last two terms in Equation 2.1 contribute to a strong interference pattern at the detector. Therefore, the noise in the hologram induced from the background environment can be reduced by dividing the hologram with the reference intensity, and the normalized hologram is given by,

$$H_N(x, y, 0) \approx 1 + \frac{\tilde{U}_R^*(X, Y, Z_D)\tilde{U}_O(X, Y, Z_D) + \tilde{U}_R(X, Y, Z_D)\tilde{U}_O^*(X, Y, Z_D)}{|\tilde{U}_R(X, Y, Z_D)|^2}. \quad (2.2)$$

The reference wave  $|\tilde{U}_R|$  can in practice be obtained from a hologram containing only the background without the object. Thus, the normalized hologram  $H_N$  contains information only related to the interference of object wave and reference wave.

After acquiring the normalized hologram, we need to use the numerical reconstruction process to simulate light travelling from the hologram and a lateral plane at distance  $z$  close to the object, so that the object information  $\tilde{U}_O$  can be estimated. In this process, the hologram, either the original or normalized, is considered as an aperture through which a virtual reference wave diffracts. This wave is back-propagated in the axial direction from the hologram to a distance  $z$  and reconstructs a virtual hologram in a new lateral plane. In this plane, the amplitude and phase information of the wave can be obtained. We can identify the patterns of the object in the reconstructed hologram, set a local region-of-

interest (ROI) to create templates containing the object and then analyze the templates to get the object information. The key to get information of the object is thus to understand how light propagates, therefore we discuss the scalar diffraction theory in the next section.

## 2.2 Scalar diffraction theory

The scalar diffraction theory is one of the most fundamental theories in digital holography and is based on the wave nature of light. Starting from Maxwell's equations, diffraction of light can be formulated with several assumptions and simplifications regarding the medium [60], [61]. For example, first, the scalar diffraction model ignores the vectorial nature of the electromagnetic field, which results in a de-coupling of electric and magnetic field components at the boundaries. Second, we assume that the medium is non-conductive and homogeneous with a constant permittivity and permeability independent to wavelength. Third, we simplify the electric and magnetic field as time-independent, so that no sources can be merged during the light propagation. Fourth, the polarization direction of the medium is isotropic and therefore the change of the field is independent to the polarization and the propagation direction of the light. From the assumptions above and Maxwell's equations, we get a scalar wave equation in the form,

$$\nabla^2 U(X, Y, Z, t) - \frac{n^2}{c^2} \frac{\partial^2 U(X, Y, Z, t)}{\partial t^2} = 0, \quad (2.3)$$

where the field  $U(X, Y, Z, t)$  represent the scalar field component at coordinate  $(X, Y, Z, t)$ ,  $\nabla^2$  is the Laplacian operator,  $n$  is the refractive index and  $c$  is the speed of light in vacuum. By assuming a monochromatic wave with wavelength  $\lambda$ , the solution to Equation 2.3 has the form,

$$U(X, Y, Z, t) = \Re\{|U(X, Y, Z)|e^{i\varphi(X, Y, Z)}e^{-i\omega t}\}, \quad (2.4)$$

where the  $\Re$  represents real part of the complex function,  $|U(X, Y, Z)|$  and  $\varphi(X, Y, Z)$  are the amplitude and phase of the scalar wave  $\tilde{U}$  at a given position  $(X, Y, Z)$ , respectively,  $\omega$  is the angular frequency of the wave and  $i$  is the imaginary unit. By combining Equation 2.3 and Equation 2.4, we get the time-independent equation,

$$(\nabla^2 + k^2)|U(X, Y, Z)|e^{i\varphi(X, Y, Z)} = 0, \quad (2.5)$$

where  $k$  is the wave number for a medium defined as  $k = n\omega/c = 2\pi n/\lambda$ . Equation 2.5 is also known as the Helmholtz equation and is the foundation of the scalar diffraction theory.

Providing that light propagation can be modeled using scalar waves, we now describe how diffraction is explained using this model. The diffraction occurs when a wave interacts with an aperture or an obstacle, or light travels through an object or medium with a varying refractive index. To find the propagating wave  $\tilde{U}$  at any point in space after interacting with an aperture, there is a solution from Gustav Kirchhoff that used Green's theorem [62]. At any point  $P$ , the method applies a closed surface boundary around  $P$  including a spherical surface connected to a planar surface directly behind an

aperture (see Figure 2.2, blue lines). Solving this surface integral using Green's theorem and Kirchhoff's boundary conditions, we arrive at the Fresnel-Kirchhoff diffraction formula,

$$\tilde{U}(P) = \frac{1}{4\pi} \iint_S \left[ \tilde{U} \frac{\partial}{\partial N} \left( \frac{e^{ikp}}{p} \right) - \frac{e^{ikp}}{p} \frac{\partial \tilde{U}}{\partial N} \right] dS, \quad (2.6)$$

where  $N$  is a vector pointing normal to the outward of surface  $S$ ,  $P$  is an arbitrary position in the coordinate  $(X, Y, Z)$ ,  $p$  is the distance from a point  $P'(X', Y')$  in the aperture to point  $P(x, y)$ . The Kirchhoff's formulation, however, has an inconsistency that requires the wave  $\tilde{U}$  and its normal derivative to be zero at the aperture. This mathematical issue can be resolved by Rayleigh-Sommerfeld formulation [58]. The Rayleigh-Sommerfeld integral describes the wave at point  $P$  produced by a surface integral over the aperture,

$$\tilde{U}(X, Y, Z) = \frac{-ikZ}{2\pi} \iint_{\text{Aperture}} \tilde{U}(X', Y', 0) \frac{e^{ikp}}{p} \left( 1 - \frac{1}{ikp} \right) dXdY, \quad (2.7)$$

where  $Z=0$  is at the aperture position, *Aperture* is the area of an aperture in a lateral plane,  $\tilde{U}(X', Y', 0)$  is the wave entering the aperture.

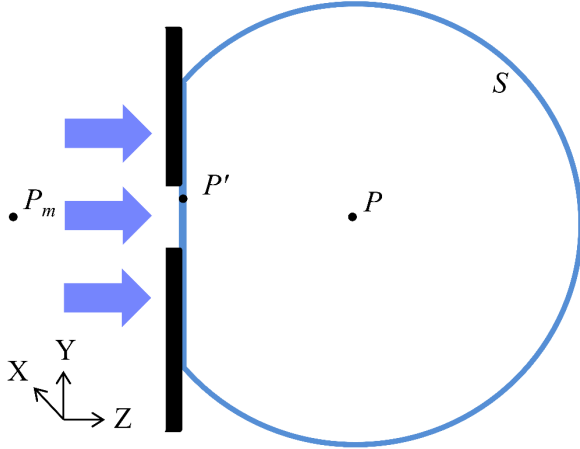


**Figure 2.2.** An example of Kirchhoff's solution describing light diffraction after an aperture. Arrows represent a wave incident from the left on the aperture that diffracts. All the points at this aperture can be seen as point sources that contribute to the new waves. The wave  $\tilde{U}$  at any point  $P$  on the right-hand side of the aperture is related to a closed surface  $S$  in blue based on the Green's theorem. The Kirchhoff's boundary conditions assume zero values on any point  $P'$  in the plane surface, including both the opaque and aperture area, for  $\tilde{U}$  and  $\partial \tilde{U} / \partial N$ . In the Rayleigh-Sommerfeld formulation, the wave at the aperture is generated from the point source  $P$  and a mirror of this source  $P_m$  on the left side of the aperture.

To derive a solution to Rayleigh-Sommerfeld integral, we first assume that  $p \gg \lambda$ , which is known as the radiation approximation. Besides, the Fresnel approximation is introduced as near-field diffraction of light close to the aperture. This condition describes a paraxial approximation, assuming the light path only deviates slightly from the center

of optical axis in the  $Z$  direction. In the end, we arrive at an approximation of Equation 2.7 in the form,

$$\tilde{U}(X, Y, Z) = \frac{-ikZ}{2\pi} \iint_{Aperture} \tilde{U}(X', Y', 0) \frac{e^{ikp}}{p} dXdY, \quad (2.8)$$

Even though the scalar diffraction theory is limited by its assumptions, as long as the object size is larger than the wavelength [58], there are experimental verification showing that the theory yields very good results if the recording of hologram is sufficiently far from the object [63]. Therefore, by using illuminations in the range of visible light, the scalar diffraction theory is sufficiently effective to approximate the light propagation for studying micro-sized cells using DHM. In the following section, we present the algorithms for constructing a virtual hologram and reconstructing virtual holograms from a real hologram based on the scalar diffraction theory using an in-line version of DHM.

### 2.3 Hologram construction and reconstruction

To simulate how light propagates from object to the hologram, we can calculate the wave function using scalar diffraction theory to construct a virtual hologram using virtual objects. We assume our reference wave to be a plane wave described by  $\exp(i(k_X X + k_Y Y + k_Z Z))$ . This assumption allows us to apply the angular spectrum method with Equation 2.8 [64]. This method represents a wave as a sum of planar waves based on the directional cosines of a vector and describe the wave propagation as the propagation of its spectrum representation in the frequency domain. The propagation of the wave  $\tilde{U}(X, Y, Z)$  is recorded as a digital hologram at position  $(X, Y, Z)$ . Based on the angular spectrum method, a Fourier transform, this hologram is constructed by,

$$\tilde{H}(X, Y, Z) = FT^{-1} \left\{ FT \left( \tilde{U}(X', Y', 0) \right) \exp \left[ \frac{i2\pi Z}{\lambda} \sqrt{1 - \left( \lambda \frac{P}{T} \right)^2 - \left( \lambda \frac{Q}{T} \right)^2} \right] \right\}, \quad (2.9)$$

where  $FT$  and  $FT^{-1}$  are the Fourier transform and the inverse of Fourier transform,  $T$  is the size of the hologram template, and  $P$  and  $Q$  are indexes in  $X$ - and  $Y$ -direction, ranging from  $-M/2$  to  $M/2$ , where  $M$  is the sampling number and  $\tilde{U}(X', Y', 0)$  is the diffracting waves from the object. The construction of holograms can be used to generate synthetic data which can be used to verify the algorithms developed for our DHM system (see Section 2.5).

In the case of hologram reconstruction, the recorded hologram  $|H(x, y, 0)|$  by the detector samples the intensity as a two-dimensional  $M \times M$  matrix in the  $x$ - and  $y$ -directions. To obtain virtual holograms from reconstruction, the hologram  $|H(x, y, 0)|$  is propagated back in the axial direction by,

$$H_r(x, y, z) = FT^{-1} \left\{ FT(|H(x, y, 0)|) \exp \left[ \frac{-i2\pi z}{\lambda} \sqrt{1 - \left( \lambda \frac{P}{T} \right)^2 - \left( \lambda \frac{Q}{T} \right)^2} \right] \right\}, \quad (2.10)$$

where the reconstructed wavefront at the distance  $z$  contains both the amplitude and phase information related to the interaction between light and the investigated object by  $H_r(x, y, z) = A(x, y, z)e^{i\phi(x, y, z)}$ . This information can be used to estimate the properties of the object absorption and phase information. To apply the reconstruction algorithm, we built an in-line version of the DHM, which is explained in the following section.

## 2.4 Experimental setup and sample preparation

We built the in-line DHM setup around an Olympus IX70 inverted microscope (Figure 2.3A), that has originally been developed for optical tweezers and microfluidic experiments [65]–[67]. We used a quasi-monochromatic light emitting diode (LED) operating at 470 nm, and we coupled this LED with an optical fiber and output collimator. Holograms were magnified by an objective and recorded using a high-speed CCD camera with RGB channels. Since the illumination LED was at 470 nm, only the B channel of the camera contains useful information.

To utilize all three channels we introduced a three-laser-wavelengths illumination system (Figure 2.3B). To reduce crosstalk noise in the camera from multiple-wavelength illuminations, we used a red (632.8 nm), a green (532 nm) and a blue laser (491 nm). Laser based illumination provide holograms with fringes at high contrast due to the spatial coherence and high light intensity. However, coherent illumination impairs the conventional DHM holograms with speckle noise, which limits the spatial resolution and image quality. To reduce speckle noise during image acquisition, we focused all three lasers on a rotating ground glass in-house [68]. By using this approach, we created a high intensity partially coherent illumination beam. To achieve better contrast in the detector plane, we spatially filtered the collimated fiber output using a pinhole and to ensure illumination with plane wavefronts, we positioned the pinhole 30 mm above to sample.

We mounted a sample chamber onto a xyz-piezo stage which could be positioned in three dimensions over a range of 100  $\mu\text{m}$  with nanometer accuracy using piezo actuators. Subsequently, we imaged the object under study using either 60 $\times$  or 100 $\times$  oil-immersion objective depending on the needed resolution. The whole setup was built in a temperature-controlled room at  $23 \pm 1^\circ\text{C}$  to ensure long-term stability and to reduce thermal drift effects in the sample [69], [70].

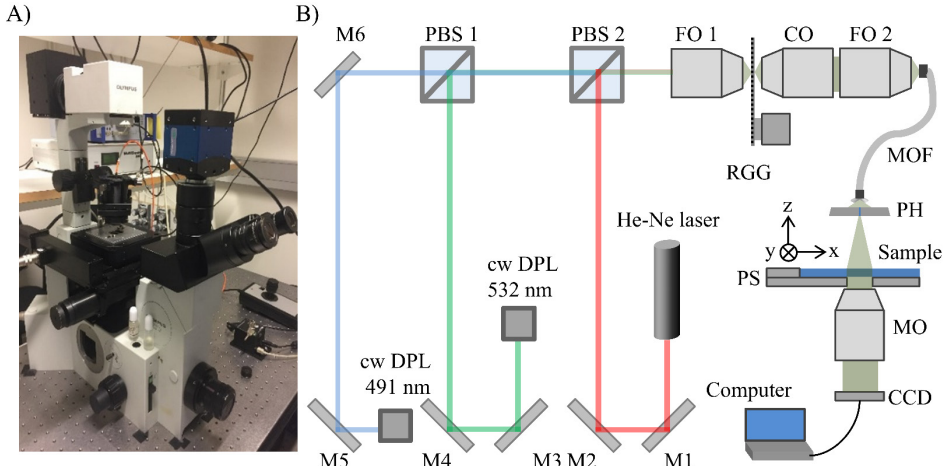


**Figure 2.3.** A) Photo of the in-line DHM system built around a conventional microscope. From the top, light is collected in a multi-mode fiber and passed through a pinhole located above the sample that can be moved by piezo actuators in 3D. A sample can be imaged by a high-speed charge-coupled device (CCD) camera. B) Schematic of the experimental setup. The abbreviations in the figure are polarized beam splitter (PBS), continuous-wave diode pumped laser (cw DPL), focusing objective (FO 1-2), collective objective (CO), magnifying objective (MO), pinhole (PH), piezo-electric stage (PS), rotating ground glass (RGG), multi-mode optical fiber (MOF) and mirrors (M1-6). The piezo-electric stage moves in 3D according to the (x, y, z) coordinates.

We made microfluidic sample channels using a sandwich construction of microscope cover slips. In these channels we introduced either particles or cells as explained in [39], [68]. But to record data on *Streptomyces coelicolor* (*S. coelicolor*) we used microfluidic plates (CellASIC ONIX) to restrict the growth in 2D.

Before conducting the measurements using real samples, we needed to verify if our algorithms and models for light propagation were correct. Therefore, we first created synthetic holograms of different samples as presented in the following section.

## 2.5 Synthetic data generation

To create synthetic DHM holograms with ground-truth data to verify the numerical reconstruction, we generated holograms for various objects, including polystyrene (PS) particles, *E. coli*, RBCs as well as random shaped objects using a custom-made MATLAB routine.

We used the Rayleigh-Sommerfeld light propagation model to generate our dataset. In the first step, we chose the simulation parameters to mimic our experimental measurements. Therefore, we set the index of refraction of the surrounding medium to  $n_m = 1.33$  (water) and the object's absorption to 0.05, since PS particles and cells are semi-transparent. We created spherical PS particles with diameter of  $1.022 \mu\text{m}$  and refractive indexes matching the laser wavelengths. We simplified the shape of *E. coli* to be an ellipsoid with a length of  $3 \mu\text{m}$  and a width of  $1 \mu\text{m}$ , and a refractive index  $n_{E. coli} = 1.38$  [67], [71], [72]. To mimic RBCs we use a Cassini shaped model with parameter values

of  $a = 2.2$ ,  $b = 2.25$ , and  $c = 0.66$  representing a  $6.3 \mu\text{m}$  wide RBC-like object with an homogeneous index of refraction  $n_{\text{RBC}} = 1.40$  [73], [74].

Second, we used these parameters as input values to our routine. Third, we simulated the wave propagation, based on Equation 2.9, by changing the distance between the object and the virtual detector in a range from  $1$  to  $50 \mu\text{m}$  with a step size of  $\Delta Z = 1 \mu\text{m}$  (Figure 2.1,  $Z$ -direction). At each  $Z$  distance, we acquired one hologram. The hologram generated by the virtual detector has a size of  $2001 \times 2001$  pixels with  $88 \text{ nm/pixel}$  and  $132 \text{ nm/pixel}$  conversion factor for hologram reconstruction according to the experimental configurations. We chose the hologram size to be large enough to avoid artifacts generated from light propagation due to the shape of the hologram template.

By using synthetic images generated from our MATLAB routine based on scalar diffraction theory, we modelled the properties of the object in a 2D lateral plane. However, real objects are in a 3D space and it is important for us to know the 3D information of the object to estimate the orientation of cells. Therefore, we used the discrete-dipole approximation (DDA) model to create synthetic hologram images of arbitrary shape since the 3D information of the object can be included in the hologram [75]. It describes a general method to compute scattering and absorption of electromagnetic waves by particles of arbitrary geometry and composition. Compared to the scalar diffraction theory, DDA considers the internal interaction and polarization, thus providing a better model for wave propagation [76]. We therefore used the DDA models to generate our datasets of *E. coli* for orientation estimation.

### 3. Diffraction Pattern Detection

#### 3.1 Features in the hologram

The diffraction patterns are one of the basic and most important features in DHM holograms. Depending on spatial position of an object in the hologram, there are in-focus object patterns with high contrast and out-of-focus diffraction patterns with distinguishing concentric fringes. From the experimental observation of PS particles, *E. coli* and RBC, the DHM holograms show connected or partially connected concentric fringes of objects (Figure 3.1A, *top*). To verify the numerical reconstruction data with experimental data, holograms from the experiment were compared to synthetic generated holograms (Figure 3.1A, *bottom*). We observed that the noise free synthetic data is similar to the experimental data. Even though the appearance of objects in the holograms are different, all the out-of-focus patterns have concentric diffraction rings with relatively high contrast in intensity. Moreover, we simulated PS particles at different axial distances (Figure 3.1B) and observed that with sufficient resolution in the hologram, the object patterns appear differently at different axial distances. Based on these observations, we were motivated to develop algorithms for detecting diffraction pattern to allow for automatic, high throughput tracking of particles and cells.

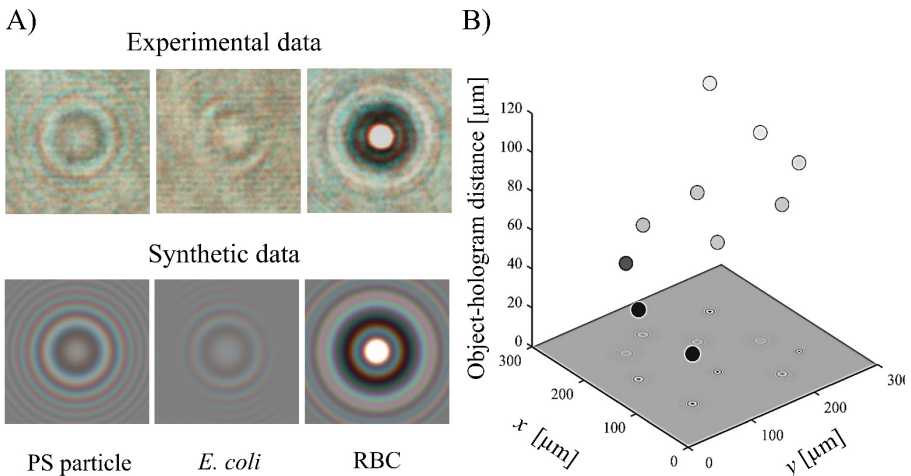


**Figure 3.1.** A) Top, templates of PS particles, *E. coli* and RBC in a real hologram (estimated  $z = 20 \mu\text{m}$ ). Bottom, synthetic templates of PS particles, *E. coli* and RBC simulated at  $z = 20 \mu\text{m}$ . B) 10 synthetic objects in 3D space and a  $300 \times 300$  hologram is created with object-hologram distance ranging from  $20 \mu\text{m}$  to  $120 \mu\text{m}$  with  $\Delta z = 10 \mu\text{m}$ . This simulation is conducted using OpticsStudio16.5 software (Zemax LLC), producing synthetic diffraction patterns of PS particles without background noise.

To detect features in the diffraction patterns we start by extracting a local region-of-interests (ROI) around each object in a hologram. To achieve this, we detect the center of concentric features to estimate the object center position in the lateral plane. Then, based on the center position and pattern size, a template is cropped from the hologram

containing concentric fringes patterns located around the template center. This template is a pre-requisite for multiple-object detection, setting up the local region for each object to allow for axial position detection, phase reconstruction and morphological analysis. However, it is a challenging task due to varying image quality. The image quality can degenerate due to the aberrations from optics, motion blur from long camera shutter times or poor resolution of the image. In fact, real holograms will also comprise uneven contrast, blurred fringes and the rings can be disconnected in some regions. Unlike the synthetic data, the noisy background in real holograms also reduces the contrast of fringes. Thus, in a DHM hologram, it is important to have a general-purpose algorithm that is robust to noise and able to detect these concentric fringes for various shaped objects with high computational efficiency.

### 3.2 Circle detection using isosceles triangles sampling

To detect diffraction patterns we developed a novel circle detection method using isosceles triangles sampling which is robust against Gaussian noise and optimized for computing performance to allow real time applications.

The algorithm is inspired from the conventional Hough transform for circle detection. However, the Hough transform is not able to validate true circles when the noise level is high. Noise in DHM holograms thus implied the need of finding a sampling strategy that has low computational complexity and high rejection rate against noise while maintaining a high probability of finding true circles. To achieve this, our algorithm used the criteria of isosceles triangles (ITs) and gradient information of the edge points [77].

We present the general idea of using isosceles triangles for circle detection in Figure 3.2A whereas the workflow for the algorithm is presented in Figure 3.2B. We denote the algorithm, ITCiD (isosceles triangles circle detection). The algorithm starts by extracting gradient information from the image. In our implementation, we filter the image with a Difference of Gaussians (DoG) kernel to obtain the image gradient magnitude and direction. This step is followed by an edge detection algorithm that evaluate strong gradient values in the image and produce a binary image to represent pixel positions related to these strong gradients. Each pair of these pixel positions in the image are then evaluated using our ITs sampling criteria. The criterion is essentially the comparison of angles to see if an isosceles triangle can be generated using the image gradient direction. However, for computational efficiency, we introduce the formula that relates the angles  $\theta_1$  and  $\theta_2$  (see Figure 3.2A) with normalized gradient vectors  $\vec{g(A)}$ ,  $\vec{g(B)}$  and the vector  $\vec{AB}$ ,  $\vec{BA}$ . This relation is given as,

$$\cos(\theta_1) = \frac{\vec{g(A)} \cdot \vec{AB}}{|\vec{AB}|}, \quad (3.1)$$

$$\cos(\theta_2) = \frac{\vec{g(B)} \cdot \vec{BA}}{|\vec{BA}|}. \quad (3.2)$$

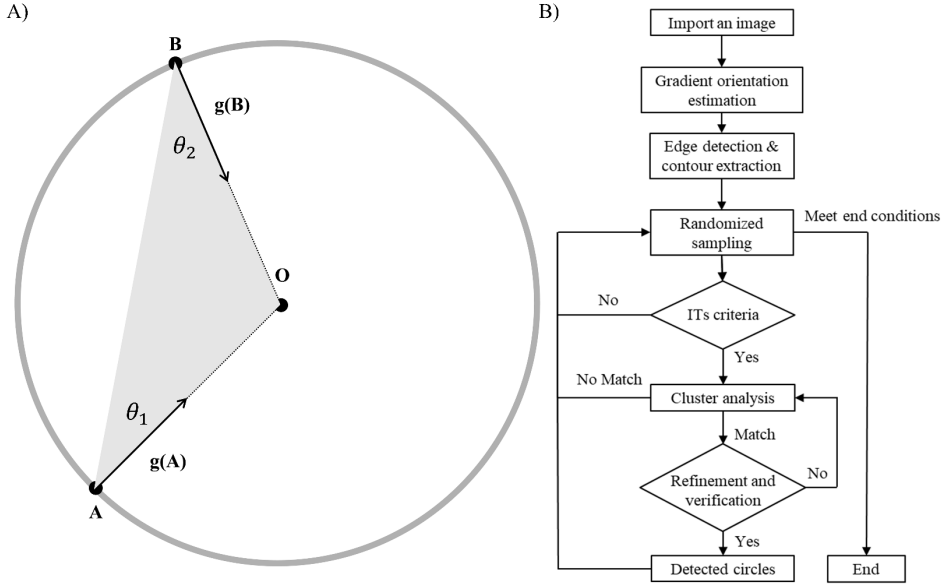


**Figure 3.2.** A) The figure shows how an isosceles triangle is detected within a circle. Using two edge pixels A and B, and their corresponding gradient vectors (solid black arrows), which points at the center point, O, an isosceles triangle AOB is found inside a circular pattern. B) The work flow of the ITCiD algorithm for multiple circles detection.

Besides, we used two criteria to ensure the correctness of angle comparison,

$$|\cos(\theta_1) - \cos(\theta_2)| \leq \Delta Th_{cos}, \quad (3.3)$$

$$\left| \overrightarrow{g(A)} \cdot \overrightarrow{g(B)} \right| < \Delta Th_g, \quad (3.4)$$

where  $\Delta Th_{cos}$  regulates the accuracy of triangles geometry and is set to a positive value,  $\Delta Th_g$  is a threshold value ranging from zero to one and refers to the minimum angles allowed between two vectors, in which zero angle value between two vectors will lead to the detection of parallel lines. In the implementation, the conditions based on Equation 3.3 and Equation 3.4 are calculated using a cascading structure to improve the sampling efficiency.

The geometrical properties of ITs have several advantages. First, ITs can be calculated from any pair of edge points on a circle, resulting in high probability for finding true circles. Second, the geometrical constrains of ITs can suppress the false-positives from background noise and unrelated textures. Third, the calculation of the ITs constraints has low computational complexity for the sampling process. The cascading structure for ITs constraint can discard many false-positives at an early stage to save computing time during the sampling. With all these features, the ITs sampling provides distinct shape discrimination for circles in the image (Figure 3.3A). We verify the algorithm using the experimental data and compared to the results from a state-of-the-art circle detection algorithm Isophote, showing the robustness of our algorithm against noise (Figure 3.3B).

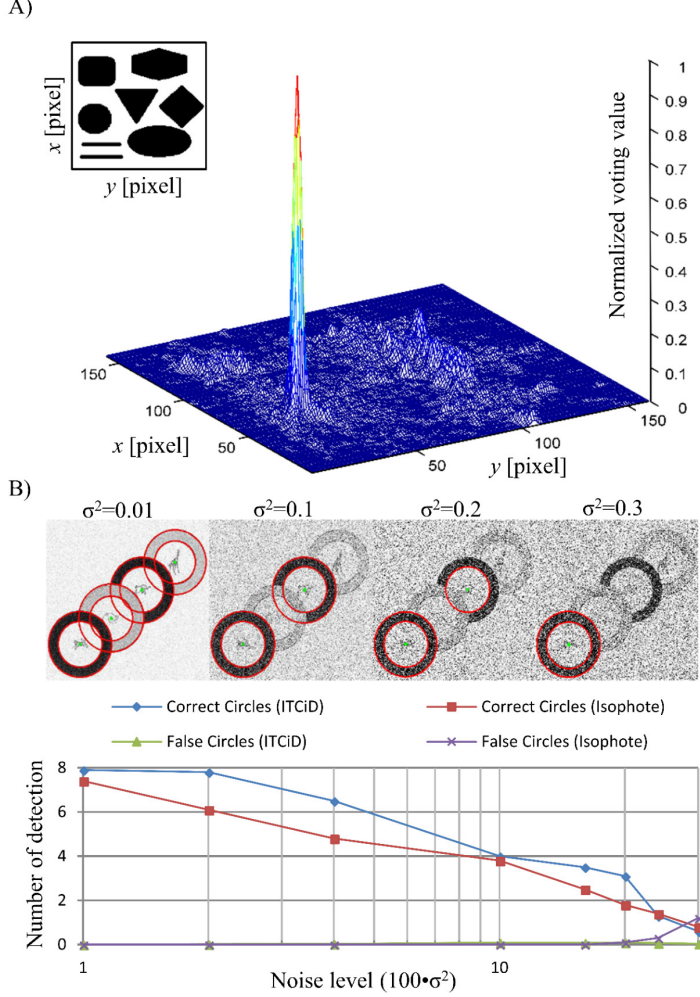


**Figure 3.3.** A) A demonstration of shape discrimination test. The ITs sampling provides a 2D distribution of voting for circle center position using a test image at the left upper corner. B) Noise tolerance experiment using a test image, "Plate". The number of correct and false circles detected in comparison to the ground truth (8 circles) for different noise levels. The red and purple lines are extracted data from [24] for comparison. The value  $\sigma$  set the standard deviation of a Gaussian distribution to control the amount of noise added to the image.

To apply the ITCiD algorithm on DHM holograms, we implemented the algorithm using a multi-scale strategy. We introduce a coarse-to-fine solution that uses a Gaussian pyramid in the scale-space, which is used in image processing algorithms to improve both performance and edge detection accuracy of blurry textures in the image [78]. For implementation efficiency, we apply down-sampling to the original image to create multiple images (Figure 3.4A). At each level of scale, we determine the particle positions from their diffraction pattern in the following way. First, the gradient of the image is calculated and used to find edges of objects. The positions of edges are converted to a

binary matrix with the same size as the original image. We then group connected edge points in the binary matrix as line segments and for each segment we apply the ITs transform. The ITs transform produces circle center positions with weight values in the binary matrix. The accumulated weight values at each position in the matrix reveal the probability of potential circle centers. By fusing all the matrixes from all the scales, the algorithm generates the final probability distribution (Figure 3.4B). This distribution is used to find the pixel position with the maximum probability value, which corresponds to the  $xy$ -center coordinates of the diffraction pattern. Note that since not all the concentric fringes from an object is needed for DHM reconstruction, we used only the center position provided by the multi-scale ITCiD algorithm to put the object in the center of a template, while the template size is determined manually with a typical pixel size of  $401 \times 401$  for computational efficiency.

Overall, ITCiD is a computational efficient algorithm that is robust against Gaussian noise. Using a multi-scale strategy for detecting the diffraction pattern center is indeed accurate and fast, able to provide high throughput results in flow chamber experiments of spherical particles (Section 4.6). This algorithm has been used to detect the diffraction pattern of some non-spherical object, such as experiments with *E. coli* (Section 5.5) and obtained correct estimation of the position following by an extra center refinement procedure. We explain the refinement procedure for finding the diffraction pattern center in the following section.

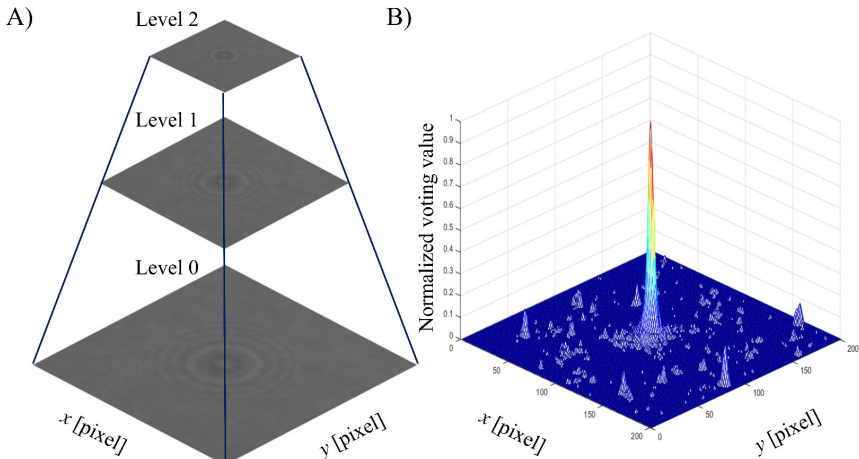


**Figure 3.4.** Demonstration of center detection using ITs transform and multi-scale strategy. A) Pyramid representation of images containing a test image with its original size at level 0 and down sampled image at level 1 and 2. The level of scales is by default set to 3 and we use the original image and two down sampled images with a factor of  $\frac{1}{2}$  and  $\frac{1}{4}$  in both length and width. B) Fused matrix for potential circle center position distribution based on the voting value calculated by ITs sampling algorithm from each level. The matrix is normalized by the maximum matrix value.

### 3.3 Refinement of the central position of an object

To analyze motion of an object, the center position must be calculated for optimal accuracy. The accuracy of single particle tracking in a 2D image is limited by both the algorithm [79] and the spatial resolution of the microscope which depends on the quality of the optics, the sample size and the illumination wavelength. To improve the detection accuracy and reach subpixel accuracy, we can refine the lateral position using the diffraction pattern. There are several algorithms developed for this purpose, e.g., Center-of-Mass (CoM) [80]; Gaussian fitting (GFit) [81]; Cross-Correlation (XCorr) [82] ; and quadrant interpolation (QI) [83]; and our proposed Circular Symmetry algorithm C-Sym [84].

The CoM algorithm locates particle centers by using an image "mass" which for example can be created by applying intensity thresholding to the image to get a binary mask. This mask separate objects from the background. The objects' coordinates are used to evaluate the center position. This algorithm is fast and simple, but very sensitive to noise in the background and light fluctuations [85]. To improve the detection accuracy and get sub-pixels accuracy, the GFit method is based on approximating the point spread function (PSF) of a particle with Gaussian functions. It is a practical method used in fluorescent microscopy data. However, this method is sensitive to changes of the position of an object in the axial direction in DHM (see Figure 3.1B) and diffraction patterns cannot be accurately described by a Gaussian distribution.

To obtain subpixel accuracy with a more relaxed constraint regarding the shape of the object than that from the GFit method, geometrical symmetry can be applied as a criterion. The XCorr algorithm locates objects by correlating different radial profiles to find the particle center of symmetry [86]. This algorithm is sensitive to noise and interference patterns from surrounding particles. The QI algorithm takes advantage of the circular geometry objects and uses image interpolation to achieve subpixel accuracy. QI requires, however, an accurate initial estimation of the particle position to perform well. Therefore, we developed the C-Sym algorithm [84]. Our C-Sym algorithm outperform the QI algorithm in accuracy and robustness against noise. C-Sym uses correlation analysis to determine the degree of symmetry at a cost of computing power. In practice, considering a trade-off between accuracy and computational efficiency, both C-Sym and XCorr algorithm are used for refining the position for subpixel accuracy in  $xy$ -plane.

# 4. Object Tracking in 3D

## 4.1 Image tracking framework

In this chapter, we discuss a general tracking framework which can be used for tracking particles in 2D and that is able to perform numerical reconstruction using DHM data to get 3D trajectories. The software workflow consists of the following four major process: pre-processing; particle center localization; tracking; and DHM reconstruction (Figure 4.1).

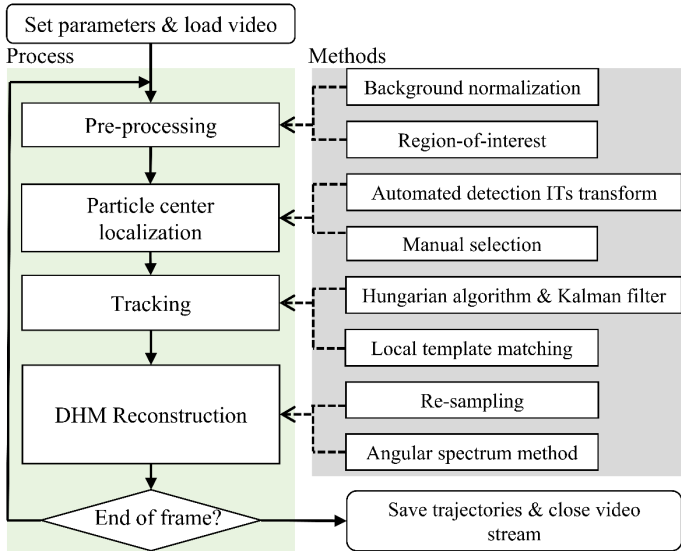


**Figure 4.1.** Block diagram of the workflow (light green column) and the class modules (grey column) for our 3D tracking software using DHM.

## 4.2 Pre-processing

The normalization procedure is a pre-requisite for processing the holograms using DHM. To reduce significant amount of noise in the hologram (Figure 4.2A), the background normalization is calculated by dividing pixel values in the hologram with corresponding values in a background image (Figure 4.2B) and then rescaling the pixel values from 0 to 1 (Figure 4.2C). To ensure numerical stability by avoiding division by zero, all intensity values in the background image are increased by a small amount, 1% of the maximum intensity. By using normalization, the processed image contains concentric diffraction rings with higher contrast than those from the original hologram, making the detection of diffraction pattern much easier and more efficient. In practice, the background image is created by averaging time-series holograms in a ROI containing moving objects, e.g., objects move in a fluidic chamber under the flow or Brownian motion of objects suspended in a fluid.

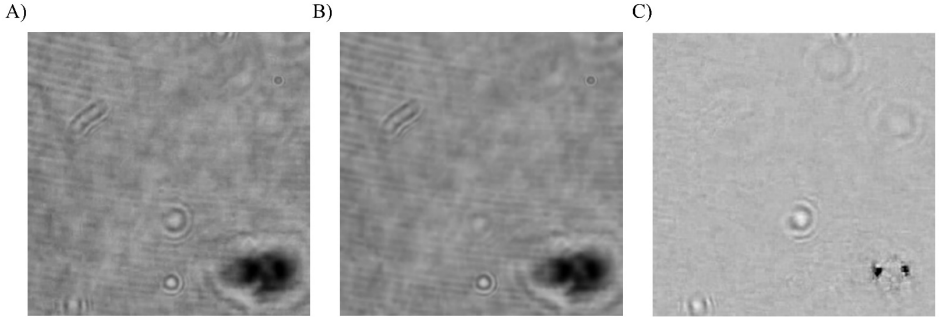


**Figure 4.2.** A) Original hologram, B) background hologram averaged over 200 frames and C) the corresponding normalized hologram. All the holograms are generated at wavelength 491 nm containing *E. coli* cells.

### 4.3 Particle center localization

An object is found by the ITs sampling algorithm and the refinement algorithm described in the previous chapter. The pattern of the object needs to be saved and centered in an image template. Since this template is used for numerical reconstruction in our framework, the major concerns for template size is the trade-off between computing performance and accuracy. In general, with a large template, the artifacts from the shape of template during the numerical reconstruction process can be ignored. However, the time needed for calculating reconstructed holograms will grow  $M^2$  as the size of the template  $M$  grows. In practice, to achieve 1  $\mu\text{m}$  axial direction accuracy and reconstruct 100 holograms ranging from 1 to 100  $\mu\text{m}$  within 1 second, we choose a typical  $401 \times 401$  template for reconstruction using a computer with an Intel® Core™ CPU i7-4770 processor.

### 4.4 Tracking

The tracking of each individual object is performed in 2D using time-series video frames recorded by the camera. The tracking in DHM refers to tracing the 3D trajectory of an object center in each frame. To acquire the trajectory correctly, the major difficulty is to make sure the same object is tracked even if other objects nearby have almost the same appearance. To ensure correct tracking, we use the Hungarian method with a Kalman filter, which provides the optimum assignment for multiple object tracking [87]–[90]. For example, assuming two objects are identified in the hologram, the Hungarian method can assign newly detected positions to these two identified objects. If there are two detections available, it is possible that two detection results are assigned as new positions for the two identified objects respectively if certain conditions are fulfilled. Depending on the implementation, these conditions set the validity of, e.g., the distances, shape and previous speed of objects, to allow a detection result to be assigned to an identified object. Moreover, if an identified object is left without a valid detection, we need to predict its position based on previous information. To achieve robust prediction, the Kalman filter uses previous trajectory information to estimate the new position of an object based on

assumptions of object's speed and acceleration in the image. In practice, the Kalman filter is efficient in tracking particle and cells that move with a constant velocity [89]. However, robust prediction of the Brownian motion of an object will lead to the stochastic particle tracking methods, which is not included in the scope of this thesis. For objects undergoing Brownian motion in a fluid, we increase the framerate of the camera and make sure the diffraction pattern detection gets valid results for every frame during the tracking. In the case when no detection results are available, we apply a simple template matching based on 2D cross-correlation of the object pattern and a local ROI in the new frame around a previously detected object center.

## 4.5 Numerical intensity reconstruction

After acquiring a hologram template with an object located at the center, the numerical reconstruction is applied to help estimate the object position in the axial direction and thus allow 3D tracking of the object. We implement the Equation 2.10 to obtain a stack of 2D intensity holograms from single template. To estimate the  $z$  position of an object, these intensity holograms are created using a fixed step size and a fixed  $z$  distance range, e.g., 100 holograms are created for PS particles with a diameter of 1  $\mu\text{m}$  using 1  $\mu\text{m}$  step size from 1 to 100  $\mu\text{m}$  in the axial direction. With sufficient number of holograms, the object position along axial direction can be estimated by finding the position of intensity maximum along the center position of holograms. The estimated position is essentially the focus of wave intensity by the object. It is a relative distance between the detector and the focus created by the intensity information of the hologram. Although the absolute distance between the object to detector is unknown, the difference of relative distances  $\Delta z$  estimated from one frame to the next can be used with the 2D tracking result to reveal the 3D trajectory.

To accurately determine the object motion, we need to verify our estimated trajectory to the real motion of the object and evaluate the accuracy of estimated positions. We conducted a calibration experiment using 1  $\mu\text{m}$  PS particles immobilized on the bottom of a coverslip in the measurement chamber. In detail, we first found stationary particles on the coverslip. Then we controlled the piezo actuators and performed a 1D scan along the  $z$  axis, covering a range between -50  $\mu\text{m}$  to 50  $\mu\text{m}$  (Figure 4.3A) around the immobilized particles on the coverslip with a step size of 1  $\mu\text{m}$ . At each piezo stage distance we acquired holograms and estimated the reconstructed distances (Figure 4.3B, spherical data points). The results show an excellent agreement between the 1  $\mu\text{m}$  piezo stage step size with the estimated step size in-between two consecutive reconstructed distances.

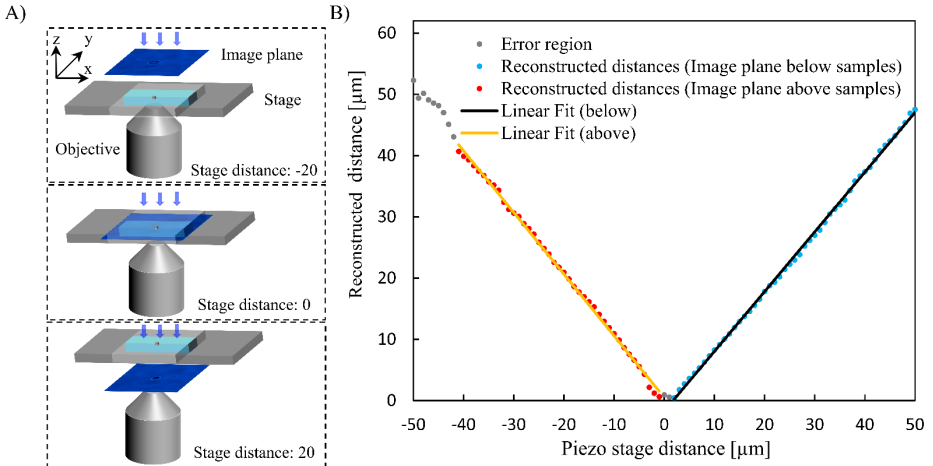


**Figure 4.3.** A) Demonstration of various positions of the sample during a 1D scan in the axial direction. In the top image, the sample is positioned between the objective and image plane. During the scan, the sample is moved through the image plane (middle), approaching its final position with the image plane located between sample and objective (bottom). The latter scenario corresponds to the classical in-line digital holography. B) Reconstruction of the focal distance for 1  $\mu\text{m}$  PS particles from experimental data acquired at 200 Hz. The reconstructed focal distance (blue data points) shows a linear relationship (black line, slope = 0.99,  $R^2 = 0.99$ ) with the piezo stage distance. Even for a scenario in which the image plane is positioned between light source and particle, UmUTracker reconstructs the particle height correctly (red data points, yellow line) showing again a linear behavior (slope = -1.03,  $R^2 = 0.99$ ).

In colloidal particle tracking experiments, we implemented our algorithms in MATLAB that utilized GPU based parallel computing. However, the reconstruction using angular spectrum method in Equation 2.10 was still a rather slow process, which is not practical for tracking of multiple particles. Thus, we made a fast implementation of the reconstruction algorithm by using the symmetry feature of spherical particles. In this case, the reconstruction is accomplished with the Rayleigh-Sommerfeld model that uses only a 1D radial intensity profile. This intensity profile is resampled using polar coordinates with its origin at the particle center. In the resampling process, sampling points are spaced by  $\Delta r_{\text{radi}}$  and  $\Delta \theta_{\text{ang}}$ , representing the minimum steps in radial and angular dimensions, respectively. At each sampling point, the intensity value is calculated using linear interpolation of two values at neighboring grid points in dimension  $x$  and  $y$ , respectively. After resampling, intensities over all angles at each radial step are averaged and the intensity profile  $I_p(radi, 0)$  of a particle from its center to a certain radius  $radi$  is created. In this process, noise and interference from nearby particles can also be reduced by means of averaging of diffraction pattern in the radial dimension. Finally, a symmetrical radial intensity profile is created by connecting the intensity profile with its mirror counterpart.

Subsequently, according to Equation 2.10 and the 1D radial intensity profiles, the reconstruction of intensity at symmetrical particle center is determined by,

$$I_R(radi, z) = FT^{-1} \left\{ FT \left( I_p(radi, 0) \right) \cdot \exp \left[ \frac{-2\pi j z}{\lambda} \sqrt{1 - \left( \lambda \frac{R}{T} \right)^2} \right] \right\}, \quad (4.1)$$

where  $R$  is a pixel index for radius ranging from  $-M/2$  to  $M/2$  and  $M$  is the total number of resampling steps. By applying the dimension reduction above, the computational cost for intensity reconstruction of particles can be reduced significantly.

## 4.6 Fluidic flow profiling

Velocimetry techniques can be used for measuring fluid velocity. We realized a 3D particle tracking velocimetry method by combining multiple-object tracking in 2D and numerical intensity reconstruction to determine the  $z$  position of an object. Using this method we conducted experiments for micro-fluidic flow profiling.

We analyzed the flow profile in a rectangular microfluidic chamber by tracking the velocity of  $1 \mu\text{m}$  particles moving at different heights in the flow. For this purpose, we use a commercially  $28 \text{ mm} \times 400 \mu\text{m} \times 100 \mu\text{m}$  (length, width, height) microfluidic bio-chip. We analyzed a  $150 \mu\text{m} \times 150 \mu\text{m} \times 100 \mu\text{m}$  ( $x, y, z$ ) volume using the hologram recorded in the  $xy$ -plane  $\sim 5 \mu\text{m}$  below the bottom surface (Figure 4.3A and a positive stage distance value). The particles were under a constant and reproducible fluidic-flow with flow rate of  $26 \pm 2 \text{ nL/s}$  in the  $x$ -direction using a microfluidic pump equipped with a  $10 \mu\text{l}$  pipette. We sampled holograms using a camera set at a frame rate of  $200 \text{ Hz}$ .

To visualize the flow cross section perpendicular to the flow in the  $x$ -direction, we collected all trajectories of tracked particles and calculated their mean position in directions  $y$  and  $z$  (Figure 4.4A). The speed in the  $x$ -direction vertical to this cross section was calculated by taking the distance between the first and last position divided by the travelling time for each trajectory.

We found that the flow velocity ranges from  $10 \mu\text{m/s}$  to  $1050 \mu\text{m/s}$  for particles close to the bottom cover slip and for particles moving in the center of the flow chamber (Figure 4.4A, blue and red data points), respectively. By fitting the velocity in the  $x$ -direction along the  $z$  axis with a polynomial of second order, the result confirms the parabolic shape which is expected for a laminar Poiseuille flow (Figure 4.4B, dashed red line). It must be mentioned that only data points below a reconstructed distance of  $55 \mu\text{m}$  are considered for fitting (Figure 4.4B, blue data points), since above this height we observed a pronounced uncertainty in our measurement results. This can be explained by the fact that diffraction patterns for particles far away from the image plane produce only diffusive diffraction patterns, reducing the accuracy of the reconstruction routine (Section 4.5). Additionally, the diffraction pattern of fast moving particles in the flow center are blurred and extended in the moving direction.

To verify our flow data and its velocity profile, we used computational fluid dynamic (CFD) simulations. Since the experimentally determined flow rate was  $26 \pm 2 \text{ nL/s}$ , we conduct the simulations for a mean flow rate of  $26 \text{ nL/s}$  and for the two extreme values, that is,  $24 \text{ nL/s}$  and  $28 \text{ nL/s}$  (Figure 4.4B, light blue line and grey area). With a maximum flow velocity of  $1150 \text{ mm/s}$  the simulation result for  $26 \text{ nL/s}$  overestimates the

experimental value by 3 %. Therefore, our flow data are better described by simulations assuming a flow rate of 24 nL/s. Furthermore, the experimentally reconstructed flow chamber height exceeds the specifications from the supplier by approximately 5%. Both deviations in maximum flow velocity and chamber height can be attributed first to a slight misalignment of coordinates between sample stage and camera in the experimental setup. Second, due to the motion blur the algorithm overestimates reconstructed distances in axial direction for fast moving particles and for those far away from the image plane. Despite these deviations, our result shows the correct flow profile in a microfluidic channel over a height range of approximately 55  $\mu\text{m}$ . Comparing to the depth of field of 60 $\times$ /1.40 objective, the DHM technique allow auto focus to extend depth of field by a factor above 100. Furthermore, we received decent agreement between measured and simulated flow profile, proving that characterization microfluidic flows using DHM is of high accuracy.

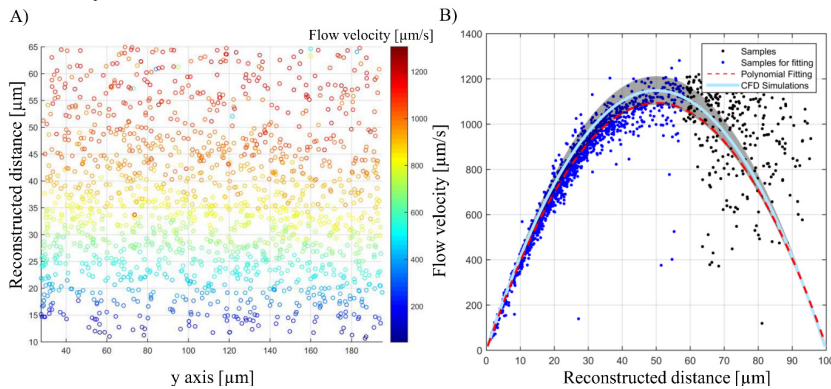


**Figure 4.4.** Microfluidic flow profiling. A) presents sampling coordinates at averaged reconstruct distance ( $z$  direction) and averaged  $y$  positions (horizontal direction which is not the flow direction) for each of the trajectory. The color code represents the averaged flow velocity at different heights. B) presents the flow profile in axial direction. Samples of averaged velocity at different axial positions are marked as dots regardless of color. A second order polynomial function is fitted to the samples ( $R^2 = 0.93$ ) in blue as dashed red line and the simulation results using CFD is presented in light blue line with error margins in grey.

Next, we applied our algorithm to fluid velocity profiling of a customized flow chamber. In this case, we fabricated a flow chamber using polydimethylsiloxane (PDMS) on a coverslip with a semi-elliptical cross section [91]. During the measurement, we created a constant and reproducible volumetric flow rate of 16 nL/s. We positioned the image plane  $\sim 5 \mu\text{m}$  below the bottom coverslip and analyzed 1500 particles in a  $272 \mu\text{m} \times 272 \mu\text{m} \times 60 \mu\text{m}$  ( $x, y, z$ ) volume. To visualize the flow profile in a cross-section perpendicular to the flow in  $x$ -direction, we interpolated the discrete point cloud to obtain a homogeneous surface representation without changing the information content and color-code the data according to the particle speed (Figure 4.5A). For the used flow rate, the flow velocity ranges from 39  $\mu\text{m/s}$  to 1766  $\mu\text{m/s}$  for particles close to the channel walls and particles moving in the center of the flow chamber, respectively.

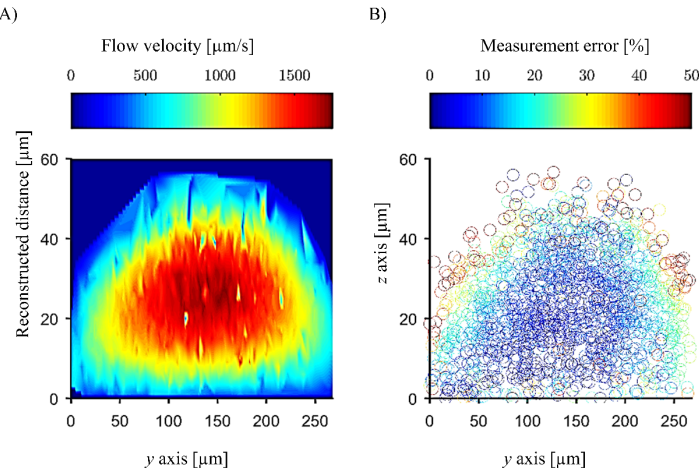


**Figure 4.5.** Micro-fluidic flow profiling of a customized flow chamber. A) presents the flow profile of a cross section perpendicular to the flow direction. The color code represents the averaged flow velocity. B) presents deviation between measured and theoretical flow profile inside the channel. We obtain best agreement in the channel middle (blue data points), whereas on the channel walls bigger deviations occur (red data points).

To assess the deviations between measured flow profile and its theoretical prediction, we determined the molded channel dimensions using light microscopy and obtain a channel width of  $380 \pm 1 \mu\text{m}$  and a channel height of  $61 \pm 7 \mu\text{m}$ . Using these channel dimensions and a volumetric flow rate of  $16.7 \text{ nL/s}$ , we calculated the theoretical flow speed in a semi-elliptical flow channel [92] and computed its deviation to the measured particles. This deviation was calculated using the mean position and velocity of each particle trajectory. We find best agreement with an average deviation of 5–10% for the center part of the channel (Figure 4.5B, blue data) and a discrepancy of 30–50% close to the channel walls and channel bottom (Figure 4.5B, yellow and red data points). Partly, we attribute these deviations to an imprecise particle localization using DHM. Particle tracking and especially intensity reconstruction to determine  $z$  position close to (near the channel bottom) and far away from (heights  $> 40 \mu\text{m}$ ) the image plane, becomes error-prone. Further, the deviation between the theoretical and experimental velocity profile can be explained by the fact that the real channel cross section is only approximately semi-elliptical. Thus, in the regions close to the channel walls the relative error becomes large as the theoretical velocity profile tend to zero while the experimental does not. Another contribution to the deviation originates from the channel shape itself. Due to its semi-elliptical shape the channel acts as a weak lens. However, the ratio between refractive indices of the water filled channel and PDMS is only 0.95, thus the deviations caused by the lensing effect are only minor. Despite these discrepancies close to the channel walls, we find excellent agreement in measured,  $1766 \mu\text{m/s}$ , and calculated maximum flow velocity,  $1835 \mu\text{m/s}$ , i.e., only a 4 % difference. Consequently, the proposed 3D particle tracking velocimetry method provides a reliable approach to profile a microfluidic channel.

## 5. Multiple-Wavelength Approach

### 5.1 Defining the object plane in DHM

In the previous chapter, we used the reconstructed hologram intensity to determine the  $z$  position of an object. This method requires that the object should focus light as a small lens. Similarly, object positions are determined by setting a focus detection criterion using either the intensity [93] or phase information [51] from the reconstruction process. To further improve the detection, K. Taute, *et al.* developed a high-throughput tracking system by fitting out-of-focus diffraction pattern with pre-recorded images at different positions [94]. N. Verrier, *et al.* use the Lorenz-Mie theory of light scattering to track colloidal particles with nanometer accuracy [95]. A. Wang, *et al.* used a discrete-dipole-approximation approach and obtained quantitative information of bacteria [96]. However, these methods require the pre-knowledge about the shape of the object and to determine the positions one need to essentially fit patterns generated from a well-defined model to experimental data. Thus, it is not practical to apply these methods to track bacteria with deformation or variation in shape. To address this problem, we developed a new multiple-wavelength method that use general criteria to detect the axial position of objects of various shapes. This method also allows for phase retrieval using in-line DHM and detects the distance from object plane to detector.

First, we recall the situation of a wave passing through an object. We define the object plane as a lateral plane where an object is simplified as a 2D shape and the axial position of this plane is set  $Z = 0$  in our coordinate system. In this plane, according to Equation 2.1 the hologram contains information of a reference wave  $\tilde{U}_R(X, Y, 0)$  representing illumination of parallel wavefronts and an object wave  $\tilde{U}_O(X, Y, 0)$  representing the scattered light passing the object.

$$\begin{aligned} H(X, Y, 0) &= |\tilde{U}_R(X, Y, 0) + \tilde{U}_O(X, Y, 0)|^2 \\ &\approx \tilde{U}_R(X, Y, 0) (1 + \tilde{\sigma}(X, Y)) \end{aligned} \quad (5.1)$$

where the scattered component is defined by a transmission function [43]  $\tilde{\sigma}(X, Y) = e^{-a(X, Y)} e^{i\Phi(X, Y)}$ , where  $a$  is the object absorption coefficient and  $\Phi$  is the phase shift caused by the object. Although the phase information in the detector is lost, by using the spatial information of the diffraction pattern, the phase information can be recovered by the Gerchberg-Saxton algorithm [97]. In the following section we present a novel algorithm using multiple-wavelength holograms and a modified Gerchberg-Saxton algorithm to recover the phase  $\Phi$  and show how this information is used for detecting the object plane.

### 5.2 Multi-wavelength Gerchberg-Saxton algorithm

To illustrate the basic concept of object plane detection and phase retrieval using the multi-wavelength Gerchberg-Saxon algorithm, we use a two-wavelength scenario for

simplicity. Note, the method can easily be expanded using several wavelengths [98]. First, the phase  $\Phi(x, y)$  in the object plane can be estimated as,

$$\Phi(x, y) = \frac{2\pi}{\lambda} [n_0(\lambda) - n_m(\lambda)] h(x, y) \quad (5.2)$$

where  $h(x, y)$  is the object thickness,  $n_0$  is the refractive index of the object and  $n_m$  is the refractive index of the surrounding medium. In the following, we assume a constant, wavelength-independent refractive index for the object and its surrounding medium. With this assumption, the phase for an object at two different wavelengths  $\lambda_1$  and  $\lambda_2$  can be related by,

$$\frac{\Phi_1(x, y)}{\Phi_2(x, y)} = \frac{\lambda_2}{\lambda_1} \quad (5.3)$$

Therefore, if the phase information is correctly retrieved in the object plane, we expect a high similarity between  $\Phi_1(x, y)$  and  $\Phi_2(x, y)$  scaled by  $\lambda_2/\lambda_1$ .

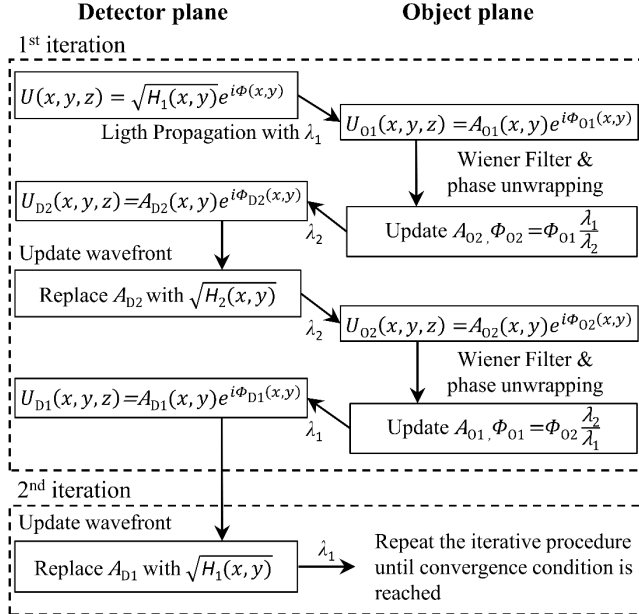


**Figure. 5.1.** The work flow of the multiple-wavelength Gerchberg-Saxton algorithm simplified for two wavelengths. Arrows indicate the direction of data flow in the algorithm. For each iteration, the wavefront propagates back and forth in-between the detector plane and a potential object plane twice.

To correctly retrieve phase information using holograms acquired at multiple wavelengths, we developed a method based on the Gerchberg-Saxton algorithm (Figure 5.1). At the first iteration, we input the holograms intensity  $H_1(x, y)$  and  $H_2(x, y)$ , acquired at different wavelengths in the detector plane. Since the detector cannot record phase information, we assign to the initial phase  $\Phi$  randomized values, e.g., we apply noise to all pixels from a normal distribution with zero mean, standard deviation of 0.01, and

maximum phase value of 0.01 rad. After setting the values for the phase, we obtain an initial wavefront  $U(x, y, z)$  and numerically propagate the wave to a potential object plane at wavelength  $\lambda_1$ . In the potential object plane, the reconstructed wavefront  $U_{O1}(x, y, z)$  is processed by using a Wiener filter to reduce noise in the phase  $\Phi_{O1}$  followed by an unwrapping algorithm [99]. Subsequently, we update  $\Phi_{O2}$  with the unwrapped  $\Phi_{O1}$  multiplied by  $\lambda_1/\lambda_2$ . The amplitude  $A_{O2}$  is set equal to  $A_{O1}$ . Based on  $A_{O2}$  and  $\Phi_{O2}$  we calculate the propagation of this wavefront at wavelength  $\lambda_2$  to the detector plane and get the wave  $U_{D2}(x, y, z)$ . A similar procedure is repeated by first replace the amplitude  $A_{D2}$  in  $U_{D2}(x, y, z)$  with the squared root of  $H_2(x, y)$ , and then propagating the wave at wavelength  $\lambda_2$  to the object plane and then propagating back to the detector plane at wavelength  $\lambda_1$ . The second iteration is the same as the first, except the  $\Phi$  is updated iteratively in the process.

This algorithm can be extended to three (or more) wavelengths to utilize the RGB channels of a CCD camera. In the three-wavelength case, we set the multiple wavelengths iterative phase retrieval procedure by starting from wavelength  $\lambda_1$  to  $\lambda_2$ ,  $\lambda_2$  to  $\lambda_3$ , and going back from  $\lambda_3$  to  $\lambda_2$ , finally reaching  $\lambda_1$  to start another iteration.

In the algorithm, we iteratively update both the amplitude and phase at the detector plane and at a potential object plane. We denote the distance between the detector and a potential object plane as  $z$ . To achieve stable amplitude and phase values at the potential object plane, we apply a fixed number of iterations, typically 20, until our convergence condition calculated from the sum of squared error between  $H_1(x, y)$  and the square of  $A_{D1}$  is below a threshold value. To find the correct object plane among potential planes, we use the input holograms and compare it with the updated amplitude reconstructed in the detector plane. If the two amplitudes are similar it is plausible that we have found the correct object plane. In the algorithm, this is realized by comparing the square of  $A_{D1}$  and  $A_{D2}$  with  $H_1(x, y)$  and  $H_2(x, y)$ , respectively, using the score  $S_D$  at each detector-object distance  $z$  as,

$$S_D(z) = \frac{1}{n} \sum_{i=1}^{n_w} Cov[H_i, A_{Di}^2], \quad (5.4)$$

where  $Cov(H, A)$  is the covariance of matrix  $H$  and  $A$ , and  $n_w$  the number of wavelengths used for reconstruction. A high score value corresponds to similar amplitudes, but it also indicates that the reconstruction of amplitude and phase has a high accuracy. In addition, based on our similarity assumption in Equation 5.3 we also check if the obtained phases from different wavelengths at a potential object plane are similar to each other by defining a similarity score  $S_O$ ,

$$S_O(z) = Cov[\Phi_{O1}, \Phi_{O2}], \quad (5.5)$$

where the unwrapped phase distribution  $\Phi_{O1}(x, y)$  and  $\Phi_{O2}(x, y)$  are related to respective wavelength,  $\lambda_1$  and  $\lambda_2$ . For multiple wavelengths,  $S_O$  is a sum of covariances of all 2-combinations from  $n_w$  wavelengths.  $S_O$  is defined to be large when two phase

distributions are similar. In our implementation, we assign a weight  $w$  on  $S_D$  and  $1-w$  on  $S_O$ , the similarity index  $S$  is given as,

$$S = w\|S_D\| + (1 - w)\|S_O\|. \quad (5.6)$$

Depending on the noise level and the contrast in a hologram,  $w$  is tuned from 0 to 1 and  $S_i$  sets the values in  $S_i$  ranging from 0 to 1. In practice, for holograms acquired at low noise level, e.g., the synthetic data containing noise only from the hologram reconstruction process,  $w$  is set to 1. For noisy conditions and low contrast, e.g., the hologram of an *E. coli*,  $w$  is set to 0.5.

### 5.3 Phase reconstruction

Since detecting object plane position is closely related to both the amplitude and phase retrieved from our method, we demonstrate its ability to extract accurate phase information from a noisy, single-shot hologram. We conducted the verification by evaluating the phase at the object plane and compared the results with the ground truth values as well as results from a multi-height phase retrieval method using 8 holograms with in-line DHM setup [46], [100].

We first analyzed the synthetic holograms for PS particles, *E. coli* and RBCs using our proposed method. We retrieve phase information using single holograms at a fixed object-detector distance  $z = 10 \mu\text{m}$  for three wavelengths and compared the obtained values with the ground truth generated from the simulation (Section 2.5). For PS particles and *E. coli* cells, our multi-wavelength Gerchberg-Saxton algorithm achieves a 99% agreement with the ground truth after 100 iterations. However, for RBCs we achieve the same accuracy for after 500 iterations due to their size and complex structure.

Second, we acquired a single hologram at  $z = 10 \mu\text{m}$  using the RGB-DHM setup (Section 2.4), and we extract the phase information for PS particles, *E. coli* cells and RBCs and compare these values to the reference phase from the simulation data. To further verify our multi-wavelength Gerchberg-Saxton algorithm, we compared the obtained phase values to the results from a well-established multi-height method [46] [100]. This method estimates the phase information by analyzing single wavelength holograms acquired at various heights along the optical axis. For that purpose, we measure holograms with their detector-object distance ranging from the object focus up to  $40 \mu\text{m}$  with a step size of  $z = 5 \mu\text{m}$  at a fixed wavelength of  $\lambda_{\text{blue}} = 491 \text{ nm}$ .

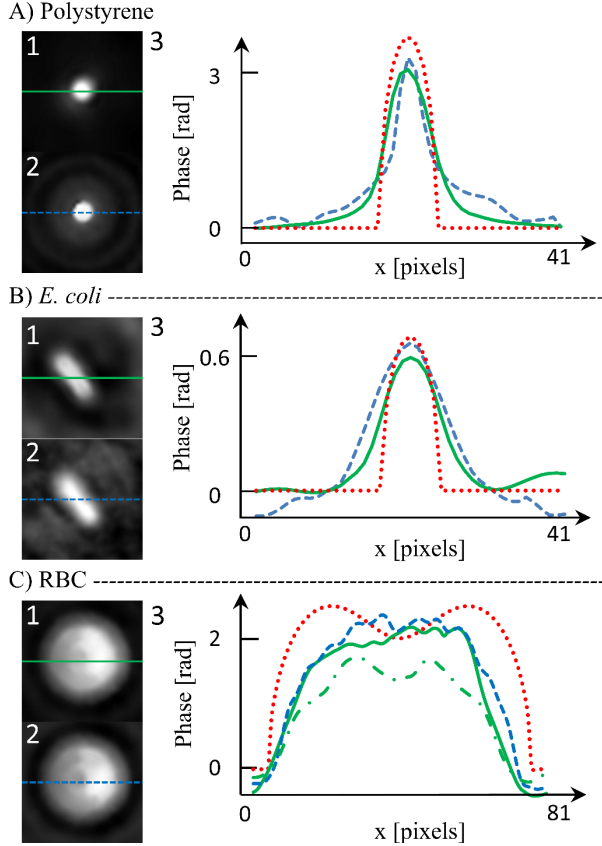


**Figure 5.2.** Comparison between phase retrieval results for A) PS particle, B) *E. coli* and C) RBC generated by using 1) the multi-wavelength Gerchberg-Saxton method and 2) the multi-height method; 3) shows the sampling of the phase profile. The green solid and dashed blue lines corresponds to our method and the multi-height method. Note that both methods used 100 iterations to obtain results for PS particle and *E. coli* data. For the RBC data, we used 200 iterations with our method. The green dashed dot line in C3 show results from our method using 100 iterations. We demonstrate here only a single image channel corresponding to a wavelength at 491 nm. The red dotted line represents the reference phase distribution from simulations for a PS particle, an *E. coli* cell and one RBC with a maximum phase value of 3.51 radian, 0.64 radian and 2.36 radian, respectively.

For PS particles, our proposed algorithm reveals a maximum phase value  $\Phi_{PS,\lambda} = 2.89 \pm 0.41$  radian, while the multi-height method produces  $\Phi_{PS,h} = 2.97 \pm 0.39$  radian (Figure 5.2A). In total, we analyzed 15 samples to get statistically reliable results and we use for each sample 100 iterations to extract the phase values. Compared to the phase value obtained in simulations, the two methods underestimate the maximum phase by  $\sim 18\%$  (multi-wavelength) and  $\sim 15\%$  (multi-height), respectively. We attribute this deviation to noise in the acquired holograms and to deviations in diameter of the used PS particles. However, more importantly, the result from our multi-wavelength Gerchberg-Saxton

algorithm differs only  $\sim 3\%$  from the multi-height approach, despite analyzing only a single hologram acquired at three wavelengths.

Next, we evaluated the phase information of 12 *E. coli* cells and 12 RBCs (Figure 5.2B-C) and compared the obtained values to the reference phase from simulations. However, due to variations in the object's shape, orientation and tilt, the simulation value might differ and is presented only as a reference. Nonetheless, the reconstructed phase information using our multi-wavelength approach (Figure 5.2B, solid green line) and the multi-height method (Figure 5.2B, dashed blue line) reproduce the phase distribution for *E. coli* similar to the reference phase, by deviating in average  $\sim 10\%$  (multi-wavelength) and  $\sim 6\%$  (multi-height) from the simulated maximum phase value. For 100 iterations the phase difference between both methods are only  $\sim 4\%$ .

For RBC data, we initially use 100 iterations and obtain a maximum phase  $\Phi_{\text{RBC}} = 1.89 \pm 0.39$  radian (multi-wavelength) and  $\Phi_{\text{RBC}} = 2.49 \pm 0.65$  radian (multi-height). However, in this case our proposed algorithm underestimates the reference phase from simulation by  $\sim 20\%$  (Figure 5.2C3, green dash dotted line) and the phase from the multi-height approach by  $\sim 5\%$  (Figure 5.2C3, blue line). This discrepancy can be resolved by doubling the iteration number during phase retrieval, resulting in a maximum phase of  $\Phi_{\text{RBC}} = 2.37 \pm 0.72$  which underestimate the reference phase by  $\sim 1\%$  (Figure 5.2C3, green solid line).

Phase reconstruction results using the in-line DHM method show that the number of iterations can be increased for better accuracy to retrieve the phase. However, for object plane detection, we found that a few iterations, e.g., 20 iterations, are sufficient for detecting the position of an object correctly.

## 5.4 Object plane position detection

To validate the capability of our multiple-wavelength Gerchberg-Saxon algorithm to find the object plane position for objects of different shapes and index of refraction at various heights, we analyzed synthetic holograms for PS particles, *E. coli* cells, and RBCs (Figure 5.3A1-C1). To find the correct object plane position  $z_o$  relative to the detector, our algorithm calculates the similarity index  $S$  (Equation 5.6) along the z direction using the reconstructed, unwrapped phase information (Figure 5.3, middle column). For that purpose, we choose manually the searching range along the z direction to be [0 60] with a step size of 1  $\mu\text{m}$  for the algorithm. After evaluating holograms at various distances from the detector, we determine the relative object plane position  $z_o$  by finding the maximum value of the similarity index  $S$  along the optical axis and plot this value against its ground truth from the simulation (Figure 5.3, right column, blue crosses). For better visibility, we plot  $z_o$  only for discrete steps of 5  $\mu\text{m}$ .

For all three test objects, we find a linear relationship between  $z_o$  and its ground truth value  $z_{\text{object}}$  from the simulation (Figure 5.3, right column, black lines). From the slope of the linear regression  $\Delta z$ , we gain a height difference between two subsequent object planes of  $\Delta z_{\text{PS, sim}} = 1.02 \pm 0.02$   $\mu\text{m}$  (PS) and  $\Delta z_{E. coli, sim} = 0.98 \pm 0.01$   $\mu\text{m}$  (*E. coli*), showing agreement with the step size parameter set in our simulations. In case of the RBC our

algorithm estimates the step size parameter from the slope of the linear regression  $\Delta z = 1.00 \pm 0.01 \mu\text{m}$  in a detector-object range from [5 20]  $\mu\text{m}$ , and  $\Delta z = 0.92 \pm 0.02 \mu\text{m}$  in a detector-object range from [5 40]  $\mu\text{m}$ . We attribute this underestimation to problems with the phase unwrapping after the reconstruction process. If an object causes a phase delay bigger than  $2\pi$ , the phase unwrapping becomes error-prone. Consequently, the signal-to-noise ratio for the similarity index  $S$  is low (Figure 5.3, RBC, middle column), leading to a less accurate object plane detection. Therefore, for our proposed algorithm we estimate the maximum object height for a wavelength of  $\lambda = 491 \text{ nm}$  to be:  $h_{\text{PS}} = 1.79 \mu\text{m}$ ,  $h_{E. \text{coli}} = 9.82 \mu\text{m}$  and,  $h_{\text{RBC}} = 7.01 \mu\text{m}$ . To enhance the performance of our algorithm for objects close to or bigger than these maximum values, we recommend using a higher optical magnification for simulations and experiments, since higher spatial resolution in the acquired hologram ensures accurate phase reconstruction, minimizing error from phase unwrapping. For this reason, we use a  $90\times$  magnification for simulations and experiments involving RBCs.

To validate our simulation results experimentally, we acquire holograms for PS particles, *E. coli* cells and RBCs using our multiple-wavelength in-line DHM setup. In detail, we first focus on an immobilized object on the coverslip  $z = 0$ . Next, we perform a 1D scan along the optical axis, covering a range from [0 50]  $\mu\text{m}$  with a step size of  $\Delta z_{\text{piezo}} = 1 \mu\text{m}$ . At each height, we acquire at least one hologram (Figure 5.3, A2-C2). From these holograms, we reconstruct, similarly to our simulations, the intensity and phase information, and estimate the similarity index  $S$  along the optical axis to determine  $z_o$ . In total, we analyzed 15 PS particles, 12 *E. coli* cells and 12 RBCs to achieve statistically reliable results.

For PS particle, *E. coli* cells and RBC, we found over the entire scan range a linear relationship between  $z_o$  and piezo stage position  $z_{\text{piezo}}$  (Figure 5.3, right column, open green spheres). From the slope of the respective linear regressions, we determine mean height difference between two subsequent object planes to:  $\Delta z_{\text{PS, exp}} = 1.02 \pm 0.01 \mu\text{m}$ ,  $\Delta z_{E. \text{coli, exp}} = 1.00 \pm 0.04 \mu\text{m}$  and,  $\Delta z_{\text{RBC, exp}} = 0.99 \pm 0.09 \mu\text{m}$ , matching the step size of the piezo stage.

Comparing these results to that from Section 4.5 using single wavelength holograms, our multi-wavelength method can provide correct axial positions at a reconstruction step of  $1 \mu\text{m}$  for  $1 \mu\text{m}$  diameter PS particles as well as cells. The single wavelength method for tracking of *E. coli* is not accurate due to the high noise level in the reconstruction process from the ‘twin image’ problem and low contrast holograms. Since the algorithm also needs very accurate center detection in  $xy$ -plane in order to get correct estimation of  $z$ -position, it requires the diffraction pattern with concentric rings. This condition is not always valid for a capsule shaped *E. coli* that can change its orientation to the plane of the detector. On the other hand, the multiple-wavelength method uses phase information to improve the reconstruction and obtained less noise. Moreover, the criteria for determining axial position in the multi-wavelength method are more robust and thus detections of axial distances from the detector (or image plane of the detector) to the object with various shape are possible. Further, since the three wavelengths are chosen to

have minimum cross-talk among the channels of our RGB-CCD, it is possible to record images at kHz framerate. In the following section we demonstrate high-speed framerate tracking of multiple cells using this multiple-wavelength approach.

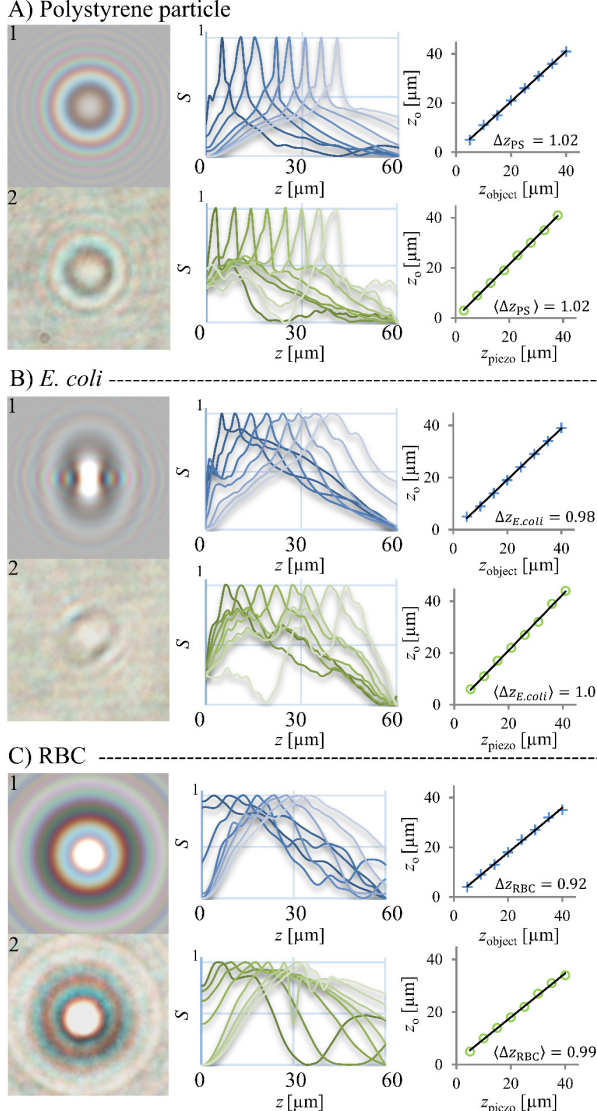


**Figure 5.3.** Synthetic and measured RGB holograms for a 1  $\mu\text{m}$  PS particle, an *E. coli*, and a RBC acquired 10  $\mu\text{m}$  from the detector plane. *Middle column.* Object plane detection using the similarity index  $S$  independent of the searching range along the  $z$  direction. Each peak corresponds to a relative object plane position  $z_o$ . *Right column.* Comparison between detected object plane position  $z_o$  and its respective ground truth  $z_{\text{object}}$  or  $z_{\text{piezo}}$ . In each case, we obtain a linear relation with a slope around  $\Delta z = 1 \mu\text{m}$  (coefficient of determination  $R^2=0.99$ ), proving that our algorithm can accurately find the object plane for samples with various shape, size and index of refraction.

## 5.5 Tracking of cells using multiple-wavelength in-line DHM

According to the object plane detection results, we can apply our algorithm for tracking suspended bacteria in a water solution. An example of this is presented in Figure 5.4. First, we apply background normalization to reduce the noise in the hologram (Section 4.2). Then, we track the position in 2D using our multi-scale ITs sampling algorithm (Section 3.2). Finally, to get the axial position we use the reconstruction algorithm for multiple-wavelength holograms (Section 5.2).

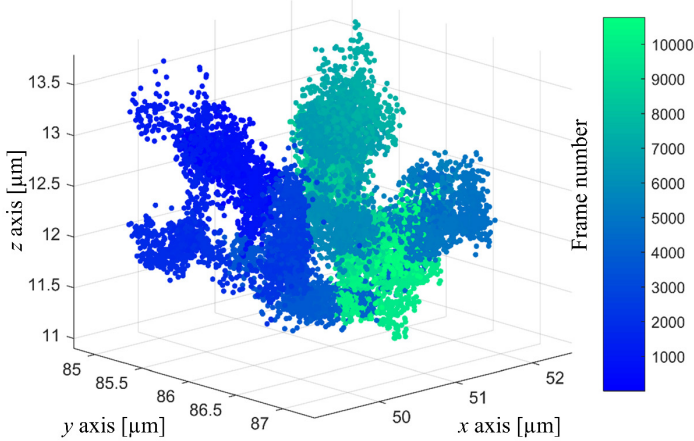


**Figure 5.4.** The 3D trajectory of a piliated *E. coli* assessed using multiple-wavelength in-line DHM. Data is recorded with a frame rate of 1kHz. 17 770 frames were analyzed for ~10 s in time. The analysis provides submicro accuracy in x, y and z direction.

We performed Brownian motion analysis in low Reynolds number condition to estimate the diffusion constant  $D$  by calculating the mean square displacement (MSD) [68], [101]. For 3D trajectories, the relation between diffusion constant and MSD is:  $\text{MSD}(\Delta t) = 6D\Delta t$ . For example, we calculated the diffusion constant to  $D = 0.05 \pm 0.01 \mu\text{m}^2/\text{s}$  for this non-motile cell located in a stationary liquid. Note that the diffusion constant obtained from a 1 μm PS particle was  $D_{\text{PS}} = 0.45 \pm 0.01 \mu\text{m}^2/\text{s}$  (Paper V). The theoretical calculation indicates that the diffusion constant estimated from this fimbriated cell is the same as an equivalent spherical particle with a diameter of 9.3 μm. This equivalent particle is larger than the size of the cell where the cell length was  $2.9 \pm 0.2 \mu\text{m}$  and cell width was  $0.8 \pm 0.2 \mu\text{m}$  measured from the image. The result from this type of measurement can be used to support our study of determining the presence of pili on a bacterium as in Paper II. However, in this case, the shape of the cell must be measured as a pre-requisite to obtain correct results for distinguishing piliated and nonpiliated bacteria.

Since the cell shape plays a very important role in many applications, e.g., it is used when estimating fluid forces on bacteria in a microfluidic flow chamber (Paper VII), tracking and image processing to extract cell morphology data is valuable. In the next chapter, we explain how to apply image segmentation methods to find the cell shape, extract backbone structures and estimate a bacterium's rotation.

# 6. Image Segmentation and Applications

## 6.1 Overview of image segmentation methods

If the object position and the distribution of phase information are estimated using in-line DHM imaging, the morphological properties of the object can be addressed using the reconstructed hologram at the object plane. In this chapter, we discuss basic image segmentation methods and introduce our segmentation algorithm for extracting backbone structures and to estimate the object's rotation.

Existing algorithms for finding object shape are mainly based on the analysis of single image. The adaptive thresholding [102] is a common method which requires no pre-knowledge of the objects and can handle significant uneven intensity distribution in the image. A multiple thresholding method have been implemented for analyzing the shape of *E. coli* [103]. However, due to its simplicity, this algorithm produces results with a lot of noise and irregular shapes, and an extra smoothing algorithm is needed to reduce the segmentation artifacts. Level-set with fast-marching is a swift implementation of active contour algorithm that can handle the topological changes of an object [104], [105]. The results from active contour algorithms have smoother boundaries than that from the adaptive thresholding method. This feature makes it easier to use the morphological thinning operation to extract the skeleton structure, and to estimate the rotation of object from the segmentation results. However, the segmentation results are dependent on the initial seed points or area selected by the user, and the segmentation areas are restricted to local regions. The watershed-based approach [106] is a popular algorithm for finding an object's contour. An advantage with the watershed transform is that it can separate two different objects that are touching each other. However, the drawback is the oversegmentation that makes merging of small fragments into an object very difficult. Research programs and software packages are also available for segmentation using single image or time-series data. CellX [107] is a powerful program for cell segmentation and optimized for objects with a clear membrane. We find however, that for objects with filamentous shape, the program cannot find seed points correctly and thus the segmentation results are incorrect. TLM-Tracker [108] is capable of tracking objects using time-lapse data only after objects have been segmented. However, the segmentation is an independent process to tracking. The results from this software are equally good as applying the geodesic active contour [105] segmentation algorithms alone.

To address the problems of finding object contours using time-lapse data and to improve the robustness of the algorithm against noise using constraints of size, edge intensity and growth rate, we develop our image segmentation algorithm by combining thresholding with a fast binary level-set method [109] which is modified to adapt to time-series data for image segmentation, and for extracting a backbone structure. The algorithm can provide robust segmentation results against noise for single object and can handle background changes between frames as well as bacterial shape deformation.

## 6.2 Level set method for time-varying objects

*E. coli* and *S. coelicolor* cells are important laboratory strains used for numerous experiments, and understanding their morphology and extracting their features are important to shed light on cellular mechanisms. Extracting their features however, requires a robust image segmentation method that can handle low contrast images, growing regions, and cell branching. A simple approach to segment an object is to use thresholding. The thresholding value can be set automatically by using a global image thresholding approach, e.g., the Otsu's method [110]. However, images acquired in a microscope often differ in quality due to uneven illumination and noise from the imaging system making segmentation difficult. In addition, results from automatic thresholding can be inaccurate due intensity fluctuations, uneven contrast of the object, and quantization errors of the image. Therefore, thresholding can only be used as a pre-step for image segmentation and feature detection if high quality results are to be obtained.

A more robust step to segment a cell is to use the level set method. We developed a modified binary level set method to handle morphology changes of cells using size constraints and past information of growth. The workflow of our binary level set method is shown in Figure 6.1 and details of the algorithm can be found in the supplementary materials of Paper IX.

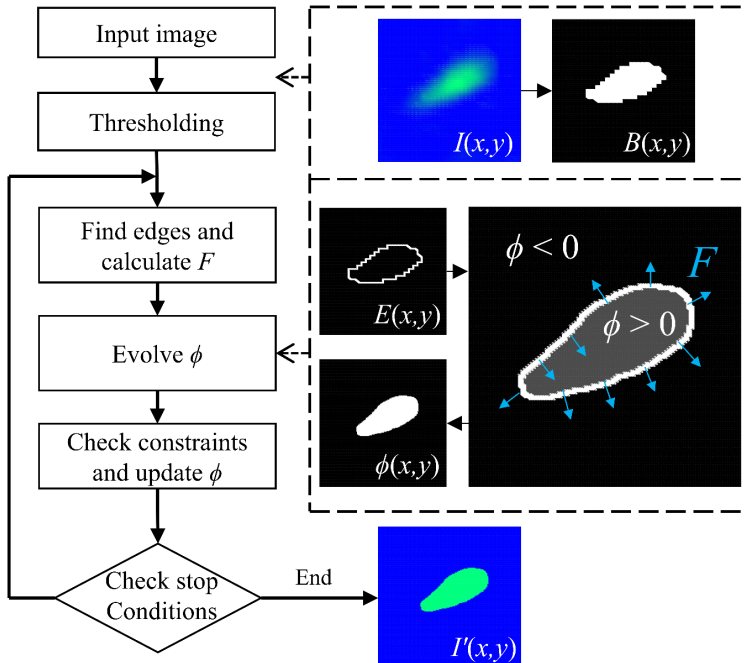


**Figure 6.1.** Illustration showing the workflow of the level set method for image segmentation. Dashed arrows relates demonstration images of processed data in each segmented step. Solid arrow indicate the flow of data in the algorithm.

First, we use the intensity of an image  $I(x, y)$  and apply thresholding to get a binary image  $B(x, y)$  of the object shape as initial status for the level set method.

Second, we define a surface  $\phi(x, y)$  to be used for segmentation. To explain the level set technique, we recall the thresholding process which sets a value to the image intensity and get segmented pixels if the pixel values are above the thresholding value. Similarly, the surface is associated with the Image  $I(x, y)$  and pixels values above 0 indicates the area of the object. However, it is important to design the algorithm to adjust the surface so that this surface can represent the shape of the object. We introduce a discrete formulation of the level set function to explain how a surface is evolved from an initial shape to the shape of the object by,

$$\phi_{j+1}(x, y) = \phi_j(x, y) + |\nabla\phi(x, y)|F_s(x, y)E_{stop}(x, y), j = 1, 2, \dots j_{max}, \quad (6.1)$$

where  $j$  represents the iteration number and  $j_{max}$  defines the maximum iteration number,  $|\nabla\phi(x, y)|$  represents the contour of the surface and the evolvement speed of the surface (denoted as  $F$  in Figure 6.1) is controlled by both  $F_s(x, y)$  and  $E_{stop}(x, y)$ . In our case, we define  $F_s(x, y)$  as sign function that produce values of -1 or 1, and define the edge stop function  $E_{stop}$  to slow down the evolvement of surface based on the image gradient values.

The evolvement of the surface start from iteration  $j = 1$  and  $\phi_1(x, y)$  is obtained from the binary  $B(x, y)$ . In a binary level set method,  $\phi$  contains only two values: -1 and 1, indicating the background and the foreground of the image, respectively. In this case,  $|\nabla\phi(x, y)|$  will have zero values for homogenous regions in  $\phi_1(x, y)$  and have non-zero values along the object contours as shown in  $E(x, y)$  in Figure 6.1. To evolve  $\phi_1(x, y)$ , we check the contour using  $E(x, y)$ , calculate  $F_s$  and  $E_{stop}$  at the contour, update the results using Equation 6.1 and update  $\phi_2$  by taking all positive values to 1 and negative values to -1. These results change the surface values and the changes corresponds to switching pixels in the contour of the object from the foreground to the background, or vice versa. According to the geodesic active contour approach [105] irregularities must be controlled during the evolution process. We use a Gaussian filter applied to the function  $\phi_2$  after the evolvement to get smoothed contour.

To achieve better accuracy in the segmentation, constraints are applied to the evolvement of the level set to avoid getting false-positive detections from the noise and the neighboring objects. These constraints can be related to the size, position, textures or the shape of the contour. By visual inspection of several experimental datasets, we made the following two simplifying assumptions to set our constraints: 1) Objects appear relatively static in a ROI of the image and 2) The growing area or deformation found from two consecutive frames is small compared to the total object size. Therefore, in every iteration we apply size constraints to split-and-merge object contours according to the surface value  $\phi$  (see the supplementary of Paper IX for more information). The surface value  $\phi$  will stop the evolvement if the stop conditions are fulfilled. The algorithm then outputs an segmented image  $I'(x, y)$  according to  $\phi$ .

To extend our segmentation algorithm using time-series data, we combine the binary level-set with adaptive thresholding and denote this approach as dynamic image segmentation. In each frame adaptive thresholding provides a new detection of object position and shape. This new object shape is compared to the previously derived results from the binary level set method, and the differences between the two shapes are found. Then the final shape is determined by evaluating the differences with the split-and-merge constraints mentioned above. With this procedure, the level set can efficiently find the initial segmentation area of the object in the new frame and thus improve the efficiency of the algorithm significantly.

From the segmentation result, the object length, width, rotation and many other shapes related information can be extracted for the study of cells. In the following sections, we provide the quantification of cells morphology using image segmentation techniques and demonstrate some important applications using the cell shape information.

### 6.3 Image segmentation of *E. coli* cells

To obtain quantitative morphological properties for *E. coli* cells suspended in a fluid, we conducted experiments by using in-line DHM imaging and processing the obtained holograms, and by apply an image segmentation algorithm to extract cell features. We first analyzed the data by tracking cells in 2D (Section 3.2), and then reconstructed holograms using multiple-wavelength algorithms (Section 5.2) to detect the axial position. Based on the position results, our multiple-wavelength approach can map the trajectory of an *E. coli* cell (Figure 6.2A) and automatically provided the phase information (Section 5.3).

The morphological information of non-spherical *E. coli* cells in a 2D image contains the length, width and angle of rotation. To obtain this information, we apply level-set segmentation to analyze the phase information. First, the values of phase distribution are rescaled in range from 0 to 1 to be used as a phase image (Figure 6.2B, *left*). The phase image works as inputs to our segmentation algorithm and the results are presented as a color-coded image, Figure 6.2B, *middle*. Based on the segmented area, we extract a backbone structure (Figure 6.2B, *right*). This backbone structure from the image is a straight forward result from morphological thinning operation in MATLAB [111]. The cell length and width were measured by calculating a major and minor axis of a best-matching ellipse through fitting of ellipses to the segmented area. To estimate the cell rotation, the orientation of the best-matching ellipse can be used. To avoid error in the rotation estimation for objects of circular shape or irregular shapes, we used an alternative way to estimate rotation by applying a linear fitting to the backbone and calculating the slope angle from the fitting function.

In our implementation, we set the rotation degrees ranging from  $-\pi/2$  to  $\pi/2$  and define 0 degree to where the cell direction is along the *y* axis. A negative rotation degree indicates that the cell direction is rotated counterclockwise. For example, based on the statistics of a cell analyzed using 200 frames, which corresponds to 0.2 s in time, we determined cell length ( $1.4 \pm 0.2 \mu\text{m}$ ), width ( $0.6 \pm 0.1 \mu\text{m}$ ) and rotation ( $-60.7 \pm 6.8$

degrees). This type of results can be used for estimating the drag force on the cells as presented in the following section. Especially, the time-series data of rotation (Figure 6.2C) are important inputs for our model to estimate the force on cells under the flow.

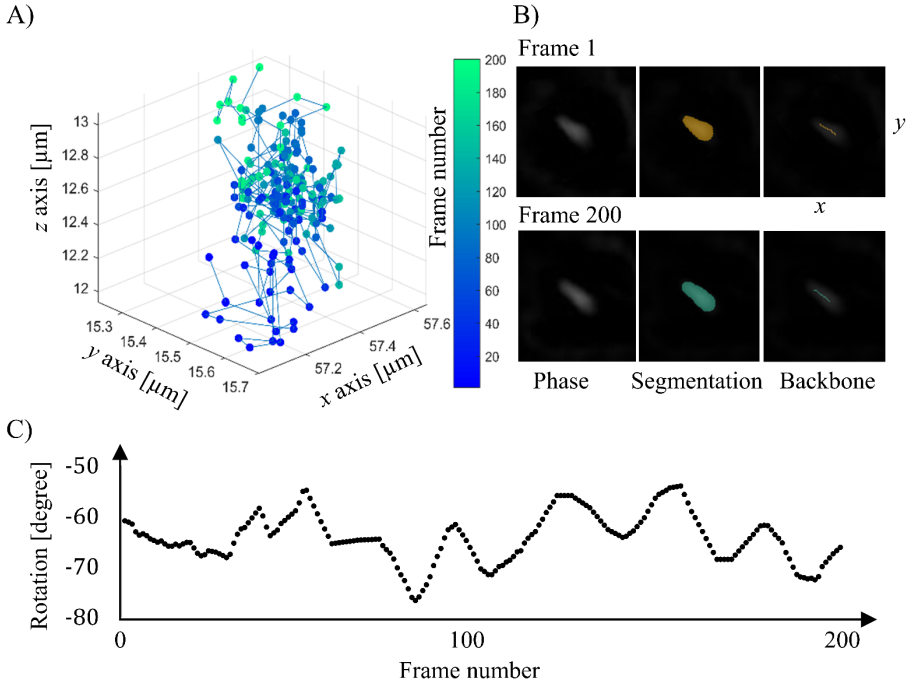


**Figure 6.2.** A) The 3D trajectory of an *E. coli* using 200 frames recorded at a frame rate of 1kHz. B) Images of rescaled phase distribution of *E. coli*, and color-coded results from our level set segmentation and backbone extraction demonstrated for frame 1 and frame 200. The x- and y-axis in the image corresponds to the x- and y-axis of the cell trajectory presented in 3D space. C) The rotation angle of the cell measured using the backbone structure with accuracy of 1 degree.

## 6.4 Estimating the drag force on *E. coli* cells

To gain a deeper understanding of the biomechanical mechanism that keeps bacteria attached to a surface under flow conditions, the hydrodynamic force acting on a specific bacterium close to a surface as a function of its geometry, size and orientation with respect to the flow must be estimated [112]. However, *E. coli* cells are capsule shaped objects that are commonly described as ellipsoids or spheres when estimating the drag force since these shapes provides easy equations to calculate the drag force. To improve on this and to develop a robust assay and analysis method for microfluidic channel experiments we needed to better understand the role of cell shape and expression of fimbriae when an *E. coli* cell is exposed to a fluid flow. Therefore, we first assessed the role of fimbriae on the hydrodynamic drag force. To acquire this, we developed a method to estimate the drag force on a single *E. coli* cell [72]. An *E. coli* cell can express a variety of fimbriae and they can express these in different numbers on the surface. We therefore grow cells

expressing different amounts of fimbriae and trapped these using an optical tweezers instrumentation [113].

Cells were first imaged in the microscope to extract their geometrical size using image processing and subsequently trapped by the optical tweezers. We oscillated the microfluidic channel, while keeping the cell stationary, and monitored the deflection of the laser beam, which then directly provides the drag force on the trapped cell. We found that fimbriae influence the drag force by increasing the drag. We found that cells expressing more fimbriae experience a higher drag than those expressing few. Therefore, by using the optical tweezers experiment, we introduce the effective diameter. It describes the fluid drag on a cell is the same as the force on a sphere with a given reference diameter.

To investigate the implication of this simplified sphere shape, we implemented several analytical models using effective diameter to calculate drag force and verify the results with CFD simulation. The equivalent radius can be found using different methods depending on shape. We considered four common models: Mean radius, Volume, Analytical and Needle. In addition, we considered an Area model that is based on wall shear stress instead of equivalent radius. We found deviations in the results from these models in comparison to the accurate CFD data we produced. Therefore, we developed an interpolation model based on capsule shape cells to more accurately calculate the hydrodynamic force on capsule-shaped cells in a micro-fluidic flow.

To verify our models, we first evaluated the shape of *E. coli* cells using image segmentation. We fitted capsule and ellipsoid-shaped models to segmented images of bacteria and found that a capsule shape gives a 4.4% better fit. This modest disparity, however, contribute to 12-15% difference in the resulting hydrodynamic force in the computational fluid dynamics CFD simulations.

For a capsule shape cells under flow, our model estimates the drag force with error less than 1% comparing to the simulation than other models in comparison. Moreover, the interpolation model can handle cell geometry as well as orientation with respect to the flow to get accurate drag force estimation. For example, according to our experiment with tethered *E. coli* to a surface (see more details in Paper VII), we estimated the cell length ( $3.6 \pm 0.2 \mu\text{m}$ ) and width ( $0.7 \pm 0.2 \mu\text{m}$ ) under the fluid flow where the shear rate was 7500 1/s with fluid density of  $1000 \text{ kg/m}^3$  and dynamic viscosity of  $0.001 \text{ kg/(s}\cdot\text{m)}$ . The cell under the flow had  $32 \pm 10$  degrees movement in rotation (angles measured between flow direction and cell rotation) during 1 s in time and the estimated drag force on the cell could range from 113 pN to 154 pN.

## 6.5 Segmentation of growing bacteria and backbone extraction

Distinctive pattern of the curves and branches in the structure of *S. coelicolor* hyphae can be observed during their growth. To quantitatively measure the feature of these growth pattern, we can use the image segmentation method to extract the shape and analyze the changes of the shape over time. To conduct the measurement, we first define the longest

path in the topological structure as the backbone pattern by excluding all the branches. This path can be extracted from our image segmentation algorithm and used for calculating the persistence length [114]. We conducted image segmentation and data analysis using our DSeg software with time-series data from DIC microscopy for *S. coelicolor* hyphae. In Figure 6.3, we present the image segmentation results and analysis of single backbone structure of *S. coelicolor* hyphae. The analysis shows the persistence length to be  $L_p = 58.56 \mu\text{m}$  for a *S. coelicolor* hyphae estimated from the  $\langle R^2 \rangle$  model which is close to the curve length  $L = 65.31 \mu\text{m}$  of the cell. This experimental result indicates the cell at this stage have high local stiffness and thus growing straight instead of getting curved. This information can be used to characterize the pattern of cells at different growing stages or external environmental factors.

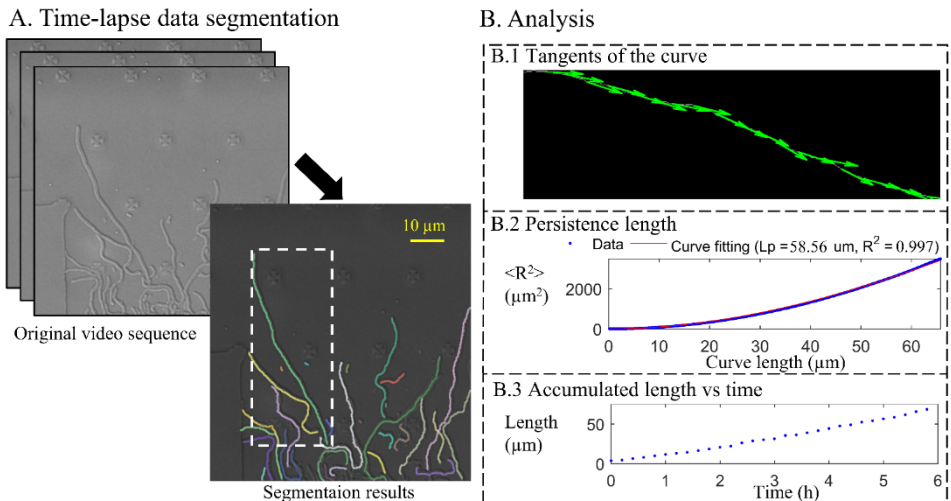


**Figure 6.3.** A) Time-lapse data of *S. coelicolor* growing from spores to hyphae structures and the segmentation results in the last frame of the video. The video data is recorded by a DIC microscopy using 100 $\times$  oil-immersion objective with numerical aperture of 1.46. We set the exposure to 100 ms and captured images every 10 minutes for approximately 24 hours using an EMCCD camera (iXonUltra ANDOR). B) Results are presented in segmented sections in panel B (dashed box). The panels show tangents of the curve extracted from the image skeleton of segmentation results, the estimation of persistence length using  $\langle R^2 \rangle$  model [115] and the accumulated length of the bacteria under 6 h growth.

# 7. Development of Software Tools

## 7.1 UmUTracker

The UmUTracker is a MATLAB based software implemented for detection of concentric-fringe-patterns and apply numerical reconstruction to track particles in 3D using data from DHM [39]. This software is based on the workflow described in Section 4.1 with 4 major steps: 1. Preprocessing, 2. Detection, 3. Tracking, 4. Numerical Reconstruction. This software is to allow fast analysis of a large number of particles and provided post-analysis interface to visualize the fluid flow profile.

The 2D tracking of particles using the software is not limited to DHM data. It can also be applied to particle or cell tracking in various dataset, e.g., images from light microscopy, DIC microscopy and fluorescent microscopy. The software offers three ways to detect objects of different shapes, including circle detection (Section 3.2), a template matching algorithm based on 2D cross-correlation, and image segmentation using morphological operations. The latest UmUTracker (version 1.2) is available at,

<https://sourceforge.net/projects/umutacker/>.

## 7.2 Capsule Cell Tracker

The Capsule Cell Tracker is a standalone software developed for applying an interpolation model to calculate the hydrodynamic force on tethered capsule-shaped cells in micro-fluidic flows near a surface [67]. In this work we present a new interpolation model with significantly better agreement compared to estimates from commonly used models and which can be used as a fast and accurate substitute for complex and computationally heavy fluid dynamic simulations. This software is optimized for tracking single cell in 2D using a time-series video and estimate the hydrodynamics force using our interpolation formula compared to the results using other 10 models [101], [116]–[118]. This force is dependent on the rotation angle of the cell and the direction of the flow. We provide the MATLAB implementation of the software with an interface available at <https://sourceforge.net/projects/capsulecelltracking/>.

## 7.3 DSeg

DSeg is an image segmentation software based on Section 6.2 and the manuscript is found in [66]. The software offers an automatic segmentation process and a manual segmentation approach. Objects in a video can be selected in the starting frame using a point-and-click function and to find their structures a thresholding algorithm can be used. After selecting the objects, the segmentation algorithm is initiated to track objects and extract their backbone structures. This software is implemented in MATLAB and the source code is available at <https://sourceforge.net/projects/dseg-software/>.

## 8. Concluding Remarks and Outlook

This work achieved two major parts for our multidisciplinary research combining image processing and biophysics: development of image processing algorithms and software tools for automated, high throughput measurements, and improvement of the in-line DHM technique; characterization of cell morphology, behavior and estimation the drag force on living cells in microfluidic channels.

In the first part, we developed an image processing ITCiD algorithm for circle detection and use it to locate centers of diffraction pattern to improve the accuracy and efficiency of object detection using DHM data. This algorithm is applied to a wide variety of circle detection tasks with better robustness against noise and high computing efficiency comparing to the state-of-the-art algorithms for circle detection (Paper I). We implemented this algorithm in a software named UmUTracker (Paper IV) that allows high throughput, automatic 3D tracking of particles. By using the DHM with 470 nm wavelength illumination, we achieved with subpixel accuracy ( $\sim 250$  nm) (Paper III) in the lateral  $xy$ -plane and submicron axial accuracy in a  $150 \times 150 \times 60 \mu\text{m}^3$  space above bottom surface in the flow chamber. The trajectories of particles are used for microfluidic flow profiling and visualization (Paper IV, Paper VI). To obtain reliable tracking of cells in 3D with high-speed recording, we improved the DHM illumination and developed a novel iterative algorithm using multiple-wavelength in-line DHM (Paper VIII) to obtain phase information and detect distance from the detector to cells. By using the illumination of wavelength at 491 nm, 532 nm and 632.8 nm, the positioning of *E. coli* can reach submicron accuracy in  $x$ -,  $y$ - and  $z$ -direction. We verified our algorithms using data of polystyrene particles (PS), *E. coli* and RBCs and applied the algorithms for detecting, tracking of cells. Better tracking results of cells in 3D allow better observation and quantitative measurement of cell morphological properties. Therefore, we developed image segmentation algorithms and implemented the DSeg software to automatically obtain high throughput morphology data of cells (Paper IX).

In the second part, the measurement of cell morphology was applied to *E. coli* cells to predict the fluid drag force using an analytical model (Paper II). Further, to study the hydrodynamic force on cells in micro-fluidic flow near a surface, we turn our analytical model to an interpolation model for better accuracy (Paper VII). Image segmentation of *E. coli* data reveals that the capsule shape modelling of *E. coli* is better than using an ellipsoid shape, and other commonly used models. Therefore, we developed a Capsule Cell Tracker software in MATLAB to apply our interpolation model for fast drag force estimation of cells in micro-fluidic flow near a surface. Finally, we show how the level set method with size constraints can be used to extract the growing speed and persistence length for quantitative characterization of growing *S. coelicolor* hyphae (Paper IX).

## **8.1 Future Applications**

Providing the 3D tracking of cells using multiple-wavelength in-line DHM and image segmentation algorithm for cell shape measurement, there are several future studies that could potentially reveal more details and answer some questions regarding bacterial adhesion.

We observed that suspending bacteria recorded in the image change appearance due to the change of their position and orientation. To quantitatively measure change of the cell position and shape, the position in x- and y-direction can be detected by ITs sampling algorithm with sub-micro accuracy and the detection of object plane for these bacteria ensure the position in z direction can also reach sub-micro accuracy with reconstruction steps smaller than 1  $\mu\text{m}$ . The orientation of object is addressed partially by measuring the rotation using the segmentation algorithm and the backbone extraction algorithm in a 2D image.

However, the angle of the object orientation with respect to the detector plane is still a challenging task. We refer this angle as the tilt of the object. Quantitative measurement of object tilt in a hologram is a complicated task. Inspired from the work in [100] where a qualitative phase retrieval technique for DHM is implemented using the deep neural networks (DNN), we started to explore the DNN to apply it for tilt estimation using DHM holograms. We used the Alex-net [119] implemented in MATLAB as the framework of our DNN and trained it with synthetic single wavelength data of *E. coli* with various shape, rotation and tilt generated from DDA simulations. In practice, our trained DNN network outputs 45 categories representing degree step of 2 for tilt estimation. In the validation of our network using a different set of synthetic holograms with ground truth values, preliminary data shows that 2 degrees accuracy can be resolved. Therefore, with proper training datasets, this approach can be used to estimate tilt of *E. coli* in real holograms. Further development of the image processing algorithms using DNN makes it possible to reveal all 5D information of the bacterial motion in fluidic flow including 3D position with rotation and tilt.

# Summary of papers

## Paper I

### A fast and robust circle detection method using isosceles triangles sampling

**H. Zhang**, K. Wiklund, and M. Andersson. Pattern Recognition 54: 218–228. (2016)

This paper presents a new circle detection method based upon randomized isosceles triangles sampling to improve the robustness of randomized circle detection in noisy conditions. It is shown that the geometrical property of isosceles triangles provides a robust criterion to find relevant edge pixels and thereby efficiently provide an estimation of the circle center and radii. Extensive experiments using both synthetic and real images were presented, and results were compared to leading state-of-the-art algorithms and showed that the proposed algorithm: are efficient in finding circles with a low number of iterations; has high rejection rate of false-positive circle candidates; and has high robustness against noise, making it adaptive and useful in many vision applications.

I developed and implemented the algorithm as well as optimized the speed by implementing both a MATLAB version and a C++ version. I performed the testing and were responsible for the comparison of our algorithm to other state-of-the-art algorithms. I was also involved in the writing of the manuscript.

## Paper II

### Detecting bacterial surface organelles on single cells using optical tweezers

J. Zakrisson, B. Singh, P. Svenmarker, K. Wiklund, **H. Zhang**, S. Hakobyan, M. Ramstedt, and M. Andersson. Langmuir 32 (18), 4521-4529 (2016)

This paper presents a method to determine the presence of pili on a single bacterium. The protocol involves imaging the bacterium to measure its size, followed by predicting the fluid drag based on its size using an analytical model, and thereafter oscillating the sample while a single bacterium is trapped by an optical tweezer to measure its effective fluid drag. Comparison between the predicted and the measured fluid drag thereby indicate the presence of pili. We verify the method using polymer coated silica microspheres and *E. coli* bacteria expressing adhesion pili. Our protocol can assist single cell studies by distinguishing between fimbriated and nonfimbriated bacteria.

In this work I carried out the analysis of bright field images of bacteria using image segmentation to extract the cell shape information of width and length. This shape information was used to calculate effective diameter to estimate the drag force on the cell.

## Paper III

### Refining particle positions using circular symmetry

A. Rodriguez, **H. Zhang**, K. Wiklund, T. Brodin, J. Klaminder, P.L. Andersson, and M. Andersson. PLoS One. 12: e0175015 (2017).

This paper presents a new algorithm, the Circular Symmetry algorithm (C-Sym), for detecting the position of a circular particle with high accuracy and precision in noisy conditions. The algorithm takes advantage of the spatial symmetry of the particle allowing for subpixel accuracy. We compare the proposed algorithm with four different methods using both synthetic and experimental datasets from colloidal, biophysical, ecological, and micro-fluidic research. The results show that C-Sym is the most accurate and precise algorithm when tracking micro-particles in all tested conditions.

I contributed to the manuscript writing, constructing synthetic datasets and implement the algorithms, CoM, *XCorr*, *QI* used for comparison particle position refinement in MATLAB for comparison.

## Paper IV

### UmUTracker: A versatile MATLAB program for automated particle tracking of 2D light microscopy or 3D digital holography data

**H. Zhang**, T. Stangner, K. Wiklund, A. Rodriguez, and M. Andersson. Computer Physics Communication 219: 390–399 (2017).

This paper presents a MATLAB program (UmUTracker) that automatically detects and tracks particles by analyzing video sequences acquired by either light microscopy or digital in-line holographic microscopy. Our program detects the 2D lateral positions of particles with an algorithm based on the isosceles triangle transform and reconstructs their 3D axial positions by a fast implementation of the Rayleigh-Sommerfeld model using a radial intensity profile. To validate the accuracy and performance of our program, we first track the 2D position of polystyrene particles using bright field and digital holographic microscopy. Second, we determine the 3D particle position by analyzing synthetic and experimentally acquired holograms. Finally, to highlight the full program features, we profile the microfluidic flow in a 100  $\mu\text{m}$  high flow chamber. This result agrees with computational fluid dynamic simulations.

My contributions were the development of algorithms for particle tracking and numerical reconstruction and implement the algorithms into a MATLAB program with a graphic user-friendly interface (GUI). I was also involved in the experimental data collection using DHM and contributed to the analysis of particles trajectories and microfluidic flow profiling using trajectories results.

## Paper V

### **Step-by-step guide to reduce spatial coherence of laser light using a rotating ground glass diffuser**

T. Stangner, **H. Zhang**, T. Dahlberg, K. Wiklund, and M. Andersson. Appl. Opt. 56: 5427 (2017).

This paper provides a method for constructing a speckle-free and high contrast laser illumination setup using a rotating ground glass diffuser driven by a stepper motor. The setup is easy to build, cheap and allows a significant light throughput of 48 %, which is 40 % higher in comparison to a single lens collector commonly used in reported setups. We validated the stability and performance of our setup in terms of image quality, motor-induced vibrations and light throughput. By using the 50x objective, high speed recording of particles with sampling rates up to 10 000 Hz are realized.

I contributed to part of the experimental work to control the step motor for rotating ground glass as well as the data analysis for characterizing the contrast in the hologram to quantify the amount of speckle noise in the image.

## Paper VI

### **3D printed water-soluble scaffolds for rapid production of PDMS micro-fluidic flow chambers**

T. Dahlberg, T. Stangner, **H. Zhang**, K. Wiklund, P. Lundberg, L. Edman, and M. Andersson. Sci. Rep 8(1):3372 (2018).

This paper reports a novel method for fabrication of three-dimensional (3D) biocompatible micro-fluidic flow chambers in polydimethylsiloxane (PDMS) by 3D-printing water-soluble polyvinyl alcohol (PVA) filaments as master scaffolds. We demonstrated the strength of our method using a regular, cheap 3D printer, and evaluated the inscription process and the channels micro-fluidic properties using image analysis and digital holographic microscopy.

In this work I carried out the analysis of the channels micro-fluidic properties using the DHM data and visualization of the fluidic flow.

## Paper VII

### A drag force interpolation model for capsule-shaped cells in fluid flows near a surface

K. Wiklund, **H. Zhang**, T. Stangner, B. Singh, E. Bullitt, and M. Andersson. *Microbiology*. 164: 483–494 (2018).

This paper presents an interpolation model to calculate the hydrodynamic force on tethered capsule-shaped cells in micro-fluidic flows near a surface. Our model is based on numerical solutions of the full Navier-Stokes equations for capsule-shaped objects considering their geometry, aspect ratio and orientation with respect to the fluid flow. The model reproduces the results from CFD simulations with an average error <0.15 % for objects with an aspect ratio up to five, and the model exactly reproduces the Goldman approximation of spherical objects close to a surface. We estimate the hydrodynamic force imposed on tethered *E. coli* cells using the interpolation model and approximate models found in the literature, e.g., one that assumes that *E. coli* are ellipsoid shaped. We fit the 2D projected area of a capsule and ellipsoid to segmented *E. coli* cells. We find that even though an ellipsoidal shape is a decent approximation of the cell shape the capsule gives 4.4 % better agreement, a small difference that corresponds to 15 % difference in hydrodynamic force.

My contributions in this work were the image segmentation of *E. coli* data and compare the capsule and ellipsoid to the segmented *E. coli* shapes. I also contributed to implementing an image processing software in MATLAB to track single cell, find its shape and apply force estimation using the interpolation formula. The software was implemented with a graphic user-friendly interface.

## Paper VIII

### Object plane detection and phase retrieval from single-shot holograms using multi-wavelength in-line holography

**H. Zhang**, T. Stangner, K. Wiklund and M. Andersson. Submitted to *Appl. Opt.* (2018).

This paper presents a novel multi-wavelength Gerchberg-Saxton algorithm to determine the object position and phase using single-shot holograms recorded in an in-line holographic microscope. For micro-sized objects, we verify the object positioning capabilities of the method for various shapes and derive the phase information using synthetic and experimental data. Experimentally, we built a compact digital in-line holographic microscopy setup around a standard optical microscope with a regular RGB-CCD camera and acquire holograms of micro-spheres, *E. coli* and red blood cells, that are illuminated using three lasers operating at 491 nm, 532 nm and 633 nm, respectively. We demonstrate that our method provides accurate object plane detection and phase

retrieval under noisy conditions, e.g., using low-contrast holograms without background normalization. This method allows for automatic positioning and phase retrieval suitable for holographic particle velocimetry, and object tracking in biophysical or colloidal research

I contributed to the development of the algorithm, implementation in MATLAB and data analysis of multiple wavelengths holograms for particles and cells. I was also involved in the data collection using the DHM setup and writing of the manuscript.

## Paper IX

### **DSeg : A dynamic image segmentation program to extract backbone patterns for filamentous bacteria and hyphae structures.**

**H. Zhang**, N. Söderholm, L. Sandblad, K. Wiklund and M. Andersson. In manuscript (2018).

This paper presents DSeg: an image analysis program designed to process time-series image data as well as single images to find multiple filamentous structures e.g., filamentous prokaryotes, yeasts and molds using a dynamic segmentation approach. DSeg automatically segments and analyzes objects, and outputs statistical data such as length, width, rotation, persistence length, growth rate and growth direction.

I contributed to the development of algorithms, the software implementation, data analysis using the software and writing of the manuscript.

# Acknowledgement

I would like to thank the people who have helped me during my PhD studies. Without your support, contribution and patience, this work would not be possible.

First, I would like to thank my supervisor, Magnus Andersson, who provides me with this research opportunity and guides me into the exciting research world. Thank you for the passionate environment you created in our group and giving me a lot of support to improve my programming and writing skills. And more importantly, I learned a lot from you as a researcher and I am truly grateful for all the valuable advices and encouragements you gave during these years.

I would like to thank my co-supervisor, Krister Wiklund, for many valuable, inspiring and fruitful discussions. You are always very kind, patient and supportive to discuss my research questions and giving me lots of hints and tips to help me overcome research problems.

I would like to express my gratefulness to the people in our group. I would like to thank Johan Zakrisson who help me a lot in the early stage of my PhD study. I want to thank Alvaro Rodriguez, Tim Stanger and Bhupender Singh for all the technical support and help in the research and having your insight and ideas about interesting and sometimes controversial topics in life. I want to thank Narges Mortezaei and Pontus Svenmarker for generous help and wish a good luck for Tobias Dahlberg for his PhD study.

I also would like to thank all the people in the physics department. Especially, I want to thank Gabriella Allansson, Hans Forsman, Jörgen Eriksson, Katarina Hassler, Nils Blix who helped me with all the administrative issue and offered technical support. I would also like to thank Alexey Klechikov, Mattias Lindh, Isak Silander, Ove Axner and Ove Andersson for giving me nice teaching experiences.

A special thanks goes to Ulrik Söderström who gave me nice advices on image processing. I would like to thank Niklas Söderholm and Linda Sandblad for collaborating on the joint project.

I would like to thank all my friends in Umeå. Especially, I would like to thank Da Wang, Yaozong Li, Chaojun Tang, Fu Xu, Xiaoying Zhang, Xiaoyi Wang, Tianyan Wang, Hui Jiang, Xiaowei Dong, Renyuan Huang, Junwen Guo, Xueen Jia, Shi Tang, Jia Wang, and Chuang Lu. We spent a lot of great and fun time together.

Finally, and most importantly, I want to express my sincere appreciation to my family: my parents and my wife. Thank you for your selfless love that support me for all these years.

# References

- [1] B. Spellberg, M. Blaser, R. J. Guidos, H. W. Boucher, J. S. Bradley, B. I. Eisenstein, D. Gerdin, R. Lynfield, L. B. Reller, J. Rex, D. Schwartz, E. Septimus, F. C. Tenover, and D. N. Gilbert, “Combating Antimicrobial Resistance: Policy Recommendations to Save Lives,” *Clin. Infect. Dis.*, vol. 52, no. suppl\_5, pp. S397–S428, May 2011.
- [2] F. Sauer, M. Mulvey, J. Schilling, J. Martinez, and S. J. Hultgren, “Bacterial pili: molecular mechanisms of pathogenesis,” *Curr. Opin.*, vol. 3, pp. 65–72, 2000.
- [3] C. R. Epler Barbercheck, E. Bullitt, and M. Andersson, “Bacterial Adhesion Pili,” in *Membrane Protein Complexes: Structure and Function*, vol. 87, 2018, pp. 1–18.
- [4] M. Andersson, E. Fällman, B. E. Uhlin, and O. Axner, “Dynamic force spectroscopy of *E. coli* P pili,” *Biophys. J.*, vol. 91, no. 7, pp. 2717–25, 2006.
- [5] M. Andersson, B. E. Uhlin, and E. Fällman, “The biomechanical properties of *E. coli* pili for urinary tract attachment reflect the host environment.,” *Biophys. J.*, vol. 93, no. 9, pp. 3008–14, 2007.
- [6] M. Castelain, A. E. Sjöström, E. Fällman, B. E. Uhlin, and M. Andersson, “Unfolding and refolding properties of S pili on extraintestinal pathogenic *Escherichia coli*.,” *Eur. Biophys. J.*, vol. 39, pp. 1105–1115, 2009.
- [7] M. Castelain, S. Ehlers, J. E. Klinth, S. Lindberg, M. Andersson, B. E. Uhlin, and O. Axner, “Fast uncoiling kinetics of F1C pili expressed by uropathogenic *Escherichia coli* are revealed on a single pilus level using force-measuring optical tweezers.,” *Eur. Biophys. J.*, vol. 40, no. 3, pp. 305–316, Mar. 2011.
- [8] M. Andersson, O. Björnham, M. Svantesson, A. Badahdah, B. E. Uhlin, and E. Bullitt, “A Structural Basis for Sustained Bacterial Adhesion: Biomechanical Properties of CFA/I Pili,” *J. Mol. Biol.*, vol. 415, no. 5, pp. 918–928, Feb. 2012.
- [9] N. Mortezaei, B. Singh, J. Zakrisson, E. Bullitt, and M. Andersson, “Biomechanical and Structural Features of CS2 Fimbriae of Enterotoxigenic *Escherichia coli*,” *Biophys. J.*, vol. 109, no. 1, pp. 49–56, Jul. 2015.
- [10] N. Mortezaei, C. R. Epler, P. P. Shao, M. Shirdel, B. Singh, A. McVeigh, B. Eric Uhlin, S. J. Savarino, M. Andersson, and E. Bullitt, “Adhesion Pili from Enterotoxigenic *Escherichia coli* Share Similar Biophysical Properties Despite Their Different Assembly Pathways,” *Microsc. Microanal.*, vol. 21, no. S3, pp. 915–916, 2015.
- [11] R. F. Thompson, M. Walker, C. A. Siebert, S. P. Muench, and N. A. Ranson, “An introduction to sample preparation and imaging by cryo-electron microscopy for structural biology,” *Methods*, vol. 100, pp. 3–15, 2016.
- [12] D. Elmlund and H. Elmlund, “Cryogenic Electron Microscopy and Single-Particle Analysis,” *Annu. Rev. Biochem.*, vol. 84, no. 1, pp. 499–517, 2015.
- [13] T. Ando, T. Uchihashi, N. Kodera, D. Yamamoto, M. Taniguchi, A. Miyagi, and H. Yamashita, “High-speed atomic force microscopy for observing dynamic

- biomolecular processes,” *J. Mol. Recognit.*, vol. 20, no. 6, pp. 448–458, 2007.
- [14] Z. Liu, L. D. Lavis, and E. Betzig, “Imaging Live-Cell Dynamics and Structure at the Single-Molecule Level,” *Mol. Cell*, vol. 58, no. 4, pp. 644–659, May 2015.
- [15] K. Ritchie and A. Kusumi, “Single-particle tracking image microscopy,” in *Methods in Enzymology*, 2003, pp. 618–634.
- [16] B. O. Leung and K. C. Chou, “Review of Super-Resolution Fluorescence Microscopy for Biology,” *Appl. Spectrosc.*, vol. 65, no. 9, pp. 967–980, Sep. 2011.
- [17] F. Zernike, “Phase contrast, a new method for the microscopic observation of transparent objects,” *Physica*, 1942.
- [18] D. Palima and J. Glückstad, “Generalised phase contrast: microscopy, manipulation and more,” *Contemp. Phys.*, vol. 51, no. 3, pp. 249–265, May 2010.
- [19] E. Horn and R. Zantl, “Phase-Contrast Light Microscopy of Living Cells Cultured in Small Volumes,” *Microsc. Anal.*, vol. 20, no. 3, pp. 5–7, 2006.
- [20] D. Way, “Principles and Applications of Differential Interference Contrast Light Microscopy,” *Microsc. Anal. Light Microsc. Suppl.*, 2006.
- [21] L. Miccio, A. Finizio, R. Puglisi, D. Balduzzi, A. Galli, and P. Ferraro, “Dynamic DIC by digital holography microscopy for enhancing phase-contrast visualization,” *Biomed. Opt. Express*, vol. 2, no. 2, p. 331, Feb. 2011.
- [22] Y. Li, J. Di, C. Ma, J. Zhang, J. Zhong, K. Wang, T. Xi, and J. Zhao, “Quantitative phase microscopy for cellular dynamics based on transport of intensity equation,” *Opt. Express*, vol. 26, no. 1, p. 586, Jan. 2018.
- [23] P. Marquet, C. Depeursinge, and P. J. Magistretti, “Exploring Neural Cell Dynamics with Digital Holographic Microscopy,” *Annu. Rev. Biomed. Eng.*, vol. 15, no. 1, pp. 407–431, Jul. 2013.
- [24] K. Lee, K. Kim, J. Jung, J. Heo, S. Cho, S. Lee, G. Chang, Y. Jo, H. Park, and Y. Park, “Quantitative Phase Imaging Techniques for the Study of Cell Pathophysiology: From Principles to Applications,” *Sensors*, vol. 13, no. 4, pp. 4170–4191, Mar. 2013.
- [25] Z. El-Schich, A. Leida Mölder, and A. Gjörloff Wingren, “Quantitative Phase Imaging for Label-Free Analysis of Cancer Cells—Focus on Digital Holographic Microscopy,” *Appl. Sci.*, vol. 8, no. 7, p. 1027, Jun. 2018.
- [26] D. GABOR, “A New Microscopic Principle,” *Nature*, vol. 161, no. 4098, pp. 777–778, May 1948.
- [27] J. W. Goodman and R. W. Lawrence, “Digital image formation from electronically detected holograms,” *Appl. Phys. Lett.*, 1967.
- [28] M. K. Kim, “Principles and techniques of digital holographic microscopy,” *SPIE Rev.*, vol. 1, no. 1, p. 018005, 2010.
- [29] O. Matoba, X. Quan, P. Xia, Y. Awatsuji, and T. Nomura, “Multimodal Imaging Based on Digital Holography,” *Proc. IEEE*, vol. 105, no. 5, pp. 906–923, May 2017.

- [30] P. Marquet, B. Rappaz, and N. Pavillon, “Quantitative phase-digital holographic microscopy: A new modality for live cell imaging,” *New Tech. Digit. Hologr.*, pp. 169–217, 2015.
- [31] D. Gao, W. Ding, M. Nieto-Vesperinas, X. Ding, M. Rahman, T. Zhang, C. Lim, and C.-W. Qiu, “Optical manipulation from the microscale to the nanoscale: fundamentals, advances and prospects,” *Light Sci. Appl.*, vol. 6, no. 9, p. e17039, Sep. 2017.
- [32] N. McReynolds, F. G. M. Cooke, M. Chen, S. J. Powis, and K. Dholakia, “Multimodal discrimination of immune cells using a combination of Raman spectroscopy and digital holographic microscopy,” *Sci. Rep.*, vol. 7, no. September 2016, p. 43631, 2017.
- [33] G. C. Antonopoulos, M. S. Rakoski, B. Steltner, S. Kalies, T. Ripken, and H. Meyer, “Experimental setup combining digital holographic microscopy (DHM) and fluorescence imaging to study gold nanoparticle mediated laser manipulation,” in *Proc. SPIE*, 2015, vol. 9336, p. 93360G.
- [34] M. Ferrando and W. E. L. Spiess, “Review: Confocal scanning laser microscopy. A powerful tool in food science Revision: Microscopía láser confocal de barrido. Una potente herramienta en la ciencia de los alimentos,” *Food Sci. Technol. Int.*, vol. 6, no. 4, pp. 267–284, Aug. 2000.
- [35] S. Satake, H. Kanamori, T. Kunugi, K. Sato, T. Ito, and K. Yamamoto, “Parallel computing of a digital hologram and particle searching for microdigital-holographic particle-tracking velocimetry,” *Appl. Opt.*, vol. 46, no. 4, p. 538, Feb. 2007.
- [36] T. Shimobaba, Y. Sato, J. Miura, M. Takenouchi, and T. Ito, “Real-time digital holographic microscopy using the graphic processing unit,” *Opt. Express*, vol. 16, no. 16, p. 11776, 2008.
- [37] N. Masuda, T. Ito, K. Kayama, H. Kono, S. Shin-ichi, T. Kunugi, and K. Sato, “Special purpose computer for digital holographic particle tracking velocimetry,” *Opt. Express*, vol. 14, no. 2, p. 587, Jan. 2006.
- [38] L. Denis, C. Fournier, T. Fournel, C. Ducottet, and D. Jeulin, “Direct extraction of the mean particle size from a digital hologram.,” *Appl. Opt.*, 2006.
- [39] H. Zhang, T. Stangner, K. Wiklund, A. Rodriguez, and M. Andersson, “UmUTracker: A versatile MATLAB program for automated particle tracking of 2D light microscopy or 3D digital holography data,” *Comput. Phys. Commun.*, vol. 219, pp. 390–399, Oct. 2017.
- [40] W. Xu, M. H. Jericho, I. a. Meinertzhausen, and H. J. Kreuzer, “Digital in-line holography for biological applications.,” *Proc. Natl. Acad. Sci. U. S. A.*, vol. 98, no. 20, pp. 11301–5, 2001.
- [41] E. Stoykova, H. Kang, and J. Park, “Twin-image problem in digital holography-a survey (Invited Paper),” *Chinese Opt. Lett.*, 2014.
- [42] D. Claus, D. Iliescu, and P. Bryanston-Cross, “Quantitative space-bandwidth product analysis in digital holography,” *Appl. Opt.*, vol. 50, no. 34, p. H116, Dec. 2011.

- [43] T. Latychevskaia and H.-W. Fink, "Solution to the Twin Image Problem in Holography," *Phys. Rev. Lett.*, vol. 98, no. 23, p. 233901, Jun. 2007.
- [44] J. Miao, P. Charalambous, J. Kirz, and D. Sayre, "Extending the methodology of X-ray crystallography to allow imaging of micrometre-sized non-crystalline specimens," *Nature*, vol. 400, no. 6742, pp. 342–344, Jul. 1999.
- [45] T. Latychevskaia and H.-W. Fink, "Simultaneous reconstruction of phase and amplitude contrast from a single holographic record," *Opt. Express*, vol. 17, no. 13, pp. 10697–10705, 2009.
- [46] A. Greenbaum and A. Ozcan, "Maskless imaging of dense samples using pixel super-resolution based multi-height lensfree on-chip microscopy," *Opt. Express*, vol. 20, no. 3, p. 3129, Jan. 2012.
- [47] X. Zhai, W.-T. Lin, H.-H. Chen, P.-H. Wang, L.-H. Yeh, J.-C. Tsai, V. R. Singh, and Y. Luo, "In-line digital holographic imaging in volume holographic microscopy," *Opt. Lett.*, vol. 40, no. 23, p. 5542, Dec. 2015.
- [48] Y. Rivenson, Y. Wu, H. Wang, Y. Zhang, A. Feizi, and A. Ozcan, "Sparsity-based multi-height phase recovery in holographic microscopy," *Sci. Rep.*, vol. 6, no. 1, p. 37862, Dec. 2016.
- [49] S. Bianchi, F. Saglimbeni, and R. Di Leonardo, "Holographic Imaging Reveals the Mechanism of Wall Entrapment in Swimming Bacteria," *Phys. Rev. X*, vol. 7, no. 1, p. 011010, 2017.
- [50] W. Luo, Y. Zhang, Z. Göröcs, A. Feizi, and A. Ozcan, "Propagation phasor approach for holographic image reconstruction," *Sci. Rep.*, vol. 6, no. 1, p. 22738, Sep. 2016.
- [51] L. Xu, M. Mater, and J. Ni, "Focus detection criterion for refocusing in multi-wavelength digital holography," *Opt. Express*, vol. 19, no. 16, p. 14779, Aug. 2011.
- [52] P. Bao, G. Situ, G. Pedrini, and W. Osten, "Lensless phase microscopy using phase retrieval with multiple illumination wavelengths," *Appl. Opt.*, vol. 51, no. 22, p. 5486, Aug. 2012.
- [53] D. W. E. Noom, D. E. Boonzaijer Flaes, E. Labordus, K. S. E. Eikema, and S. Witte, "High-speed multi-wavelength Fresnel diffraction imaging," *Opt. Express*, vol. 22, no. 25, p. 30504, Dec. 2014.
- [54] M. Sanz, J. A. Picazo-Bueno, J. García, and V. Micó, "Improved quantitative phase imaging in lensless microscopy by single-shot multi-wavelength illumination using a fast convergence algorithm," *Opt. Express*, vol. 23, no. 16, p. 21352, Aug. 2015.
- [55] N. E. Farthing, R. C. Findlay, J. F. Jikeli, P. B. Walrad, M. A. Bees, and L. G. Wilson, "Simultaneous two-color imaging in digital holographic microscopy," *Opt. Express*, vol. 25, no. 23, p. 28489, Nov. 2017.
- [56] Á. Barroso Peña, B. Kemper, M. Woerdemann, A. Vollmer, S. Ketelhut, G. von Bally, and C. Denz, "Optical tweezers induced photodamage in living cells quantified with digital holographic phase microscopy," in *SPIE Proceedings*, 2012, vol. 8427, no. May, p. 84270A.

- [57] A. De Angelis, S. Managò, M. A. Ferrara, M. Napolitano, G. Coppola, and A. C. De Luca, “Combined Raman Spectroscopy and Digital Holographic Microscopy for Sperm Cell Quality Analysis,” *J. Spectrosc.*, vol. 2017, pp. 1–14, 2017.
- [58] J. W. Goodman, *Introduction to Fourier Optics* (3rd ed.). Roberts & Company, 2005.
- [59] D. O’Shea, “Scalar Diffraction Theory,” *Diffractive Opt. Des. Fabr. test*, 2004.
- [60] B. Mahon, “How Maxwell’s equations came to light,” *Nat. Photonics*, vol. 9, no. 1, pp. 2–4, Jan. 2015.
- [61] J. C. Maxwell, “A Dynamical Theory of the Electromagnetic Field,” *Philos. Trans. R. Soc. London*, vol. 155, pp. 459–512, Jan. 1865.
- [62] W. . Steen, “Principles of Optics M. Born and E. Wolf, 7th (expanded) edition, Cambridge University Press, Cambridge, 1999, 952pp. 37.50/US \$59.95, ISBN 0-521-64222-1,” *Opt. Laser Technol.*, vol. 32, no. 5, p. 385, Jul. 2000.
- [63] S. Chi and Q. Guo, “Vector theory of self-focusing of an optical beam in Kerr media.,” *Opt. Lett.*, 1995.
- [64] J. A. Ratcliffe, “Some Aspects of Diffraction Theory and their Application to the Ionosphere,” *Reports Prog. Phys.*, vol. 19, no. 1, p. 188, 1956.
- [65] E. Fällman, S. Schedin, J. Jass, M. Andersson, B. E. Uhlin, and O. Axner, “Optical tweezers based force measurement system for quantitating binding interactions: system design and application for the study of bacterial adhesion,” *Biosens. Bioelectron.*, vol. 19, no. 11, pp. 1429–1437, 2004.
- [66] H. Zhang, N. Soderholm, L. Sandblad, K. Wiklund, and M. Andersson, “DSeg: A dynamic image segmentation program to extract backbone patterns for filamentous bacteria and hyphae structures,” *bioRxiv*, Jan. 2018.
- [67] K. Wiklund, H. Zhang, T. Stangner, B. Singh, E. Bullitt, and M. Andersson, “A drag force interpolation model for capsule-shaped cells in fluid flows near a surface,” *Microbiology*, pp. 1–12, Mar. 2018.
- [68] T. Stangner, H. Zhang, T. Dahlberg, K. Wiklund, and M. Andersson, “A step-by-step guide to reduce spatial coherence of laser light using a rotating ground glass diffuser,” *Appl. Opt.*, vol. 56, no. 24, pp. 1–7, 2017.
- [69] M. Andersson, E. Fällman, B. E. Uhlin, and O. Axner, “Force measuring optical tweezers system for long time measurements of P pilus stability,” *Proc. SPIE*, vol. 6088, pp. 286–295, 2006.
- [70] M. Andersson, F. Czerwinski, and L. B. Oddershede, “Optimizing active and passive calibration of optical tweezers,” *J. Opt.*, vol. 13, no. 4, p. 044020, Apr. 2011.
- [71] A. E. Balaev, K. N. Dvoretski, and V. A. Doubrovski, “Refractive index of escherichia coli cells,” in *Proc. SPIE 4707, Saratov Fall Meeting 2001: Optical Technologies in Biophysics and Medicine III, (16 July 2002)*, 2002, vol. 4707, pp. 253–260.
- [72] J. Zakrisson, B. Singh, P. Svenmarker, K. Wiklund, H. Zhang, S. Hakobyan, M. Ramstedt, and M. Andersson, “Detecting Bacterial Surface Organelles on Single

- Cells Using Optical Tweezers,” *Langmuir*, vol. 32, no. 18, pp. 4521–4529, May 2016.
- [73] T. Wriedt, J. Hellmers, E. Eremina, and R. Schuh, “Light scattering by single erythrocyte: Comparison of different methods,” *J. Quant. Spectrosc. Radiat. Transf.*, vol. 100, no. 1–3, pp. 444–456, Jul. 2006.
- [74] J. Zakrisson, S. Schedin, and M. Andersson, “Cell shape identification using digital holographic microscopy,” *Appl. Opt.*, vol. 54, no. 24, pp. 7442–7448, 2015.
- [75] B. T. Draine and P. J. Flatau, “Discrete-Dipole Approximation For Scattering Calculations,” *J. Opt. Soc. Am. A*, vol. 11, no. 4, p. 1491, Apr. 1994.
- [76] M. A. Yurkin and A. G. Hoekstra, “The discrete-dipole-approximation code ADDA: Capabilities and known limitations,” *J. Quant. Spectrosc. Radiat. Transf.*, vol. 112, no. 13, pp. 2234–2247, 2011.
- [77] H. Zhang, K. Wiklund, and M. Andersson, “A fast and robust circle detection method using isosceles triangles sampling,” *Pattern Recognit.*, vol. 54, no. C, pp. 218–228, Jun. 2016.
- [78] T. Lindeberg, “Scale-space theory : A basic tool for analysing structures at different scales,” *J. Appl. Stat.*, vol. 21, no. 1–2, p. 225-, 1994.
- [79] P. Hanninen and P. Hänninen, “Light microscopy: beyond the diffraction limit.,” *Nature*, 2002.
- [80] R. N. Ghosh and W. W. Webb, “Automated detection and tracking of individual and clustered cell surface low density lipoprotein receptor molecules.,” *Biophys. J.*, vol. 66, no. 5, pp. 1301–1318, 1994.
- [81] R. S. Wilson, L. Yang, A. Dun, A. M. Smyth, R. R. Duncan, C. Rickman, and W. Lu, “Automated single particle detection and tracking for large microscopy datasets,” *R. Soc. Open Sci.*, vol. 3, no. 5, p. 160225, 2016.
- [82] J. Gelles, B. J. Schnapp, and M. P. Sheetz, “Tracking kinesin-driven movements with nanometre-scale precision.,” *Nature*, vol. 331, no. 6155. pp. 450–453, 1988.
- [83] M. van Loenhout, J. Kerssemakers, I. De Vlaminck, and C. Dekker, “Non-Bias-Limited Tracking of Spherical Particles, Enabling Nanometer Resolution at Low Magnification,” *Biophys. J.*, vol. 102, no. 10, pp. 2362–2371, 2012.
- [84] A. Rodriguez, H. Zhang, K. Wiklund, T. Brodin, J. Klaminder, P. L. Andersson, and M. Andersson, “Refining particle positions using circular symmetry,” *PLoS One*, vol. 12, no. 4, p. e0175015, 2017.
- [85] A. J. Berglund, M. D. McMahon, J. J. McClelland, and J. A. Liddle, “Fast, bias-free algorithm for tracking single particles with variable size and shape.,” *Opt. Express*, 2008.
- [86] C. Gosse and V. Croquette, “Magnetic tweezers: micromanipulation and force measurement at the molecular level,” *Biophys J*, 2002.
- [87] H. W. Kuhn, “The Hungarian method for the assignment problem,” *Nav. Res. Logist. Q.*, vol. 2, no. 1–2, pp. 83–97, 1955.

- [88] R. E. Kalman, “A New Approach to Linear Filtering and Prediction Problems,” *J. Basic Eng.*, vol. 82, no. 1, p. 35, 1960.
- [89] A. Rodriguez, H. Zhang, J. Klaminder, T. Brodin, and M. Andersson, “ToxId: an efficient algorithm to solve occlusions when tracking multiple animals,” *Sci. Rep.*, vol. 7, no. 1, p. 14774, Dec. 2017.
- [90] A. Rodriguez, H. Zhang, J. Klaminder, T. Brodin, P. L. Andersson, and M. Andersson, “ToxTrac : A fast and robust software for tracking organisms,” *Methods Ecol. Evol.*, vol. 9, no. 3, pp. 460–464, Mar. 2018.
- [91] T. Dahlberg, T. Stangner, H. Zhang, K. Wiklund, P. Lundberg, L. Edman, and M. Andersson, “3D printed water-soluble scaffolds for rapid production of PDMS micro-fluidic flow chambers,” *Sci. Rep.*, vol. 8, no. 1, p. 3372, Dec. 2018.
- [92] R. S. Allassar and M. Abushoshah, “Hagen–Poiseuille Flow in Semi-Elliptic Microchannels,” *J. Fluids Eng.*, 2012.
- [93] Y. J. Choo and B. S. Kang, “The characteristics of the particle position along an optical axis in particle holography,” *Meas. Sci. Technol.*, vol. 17, no. 4, pp. 761–770, Apr. 2006.
- [94] K. M. Taute, S. Gude, S. J. Tans, and T. S. Shimizu, “High-throughput 3D tracking of bacteria on a standard phase contrast microscope,” *Nat. Commun.*, vol. 6, no. May, pp. 1–9, 2015.
- [95] N. Verrier, C. Fournier, and T. Fournel, “3D tracking the Brownian motion of colloidal particles using digital holographic microscopy and joint reconstruction,” *Appl. Opt.*, vol. 54, no. 16, p. 4996, Jun. 2015.
- [96] A. Wang, R. F. Garmann, and V. N. Manoharan, “Tracking *E. coli* runs and tumbles with scattering solutions and digital holographic microscopy,” *Opt. Express*, vol. 24, no. 21, pp. 23719–23725, 2016.
- [97] R. W. Gerchberg and W. O. Saxton, “A practical algorithm for the determination of phase from image and diffraction plane pictures,” *Optik (Stuttg.)*, 1972.
- [98] H. Zhang, T. Stangner, K. Wiklund, and M. Andersson, “Object Plane Detection and Phase Retrieval from Single-Shot Holograms using Multi-Wavelength In-Line Holography,” *ArXiv*, pp. 1–7, Aug. 2018.
- [99] D. C. Ghiglia and L. A. Romero, “Robust two-dimensional weighted and unweighted phase unwrapping that uses fast transforms and iterative methods,” *J. Opt. Soc. Am. A*, vol. 11, no. 1, p. 107, Jan. 1994.
- [100] Y. Rivenson, Y. Zhang, H. Günaydin, D. Teng, and A. Ozcan, “Phase recovery and holographic image reconstruction using deep learning in neural networks,” *Light Sci. Appl.*, vol. 7, no. 2, p. 17141, Feb. 2018.
- [101] R. A. Siegel, “Random walks in biology,” *J. Control. Release*, 1994.
- [102] D. Bradley and G. Roth, “Adaptive Thresholding using the Integral Image,” *J. Graph. Tools*, vol. 12, no. 2, pp. 13–21, 2007.
- [103] S. K. Sadanandan, Ö. Baltekin, K. E. G. Magnusson, A. Boucharin, P. Ranefall, J. Jaldén, J. Elf, and C. Wählby, “Segmentation and Track-Analysis in Time-Lapse Imaging of Bacteria,” *IEEE J. Sel. Top. Signal Process.*, vol. 10, no. 1, pp.

174–184, 2016.

- [104] D. Adalsteinsson and J. A. Sethian, “The Fast Construction of Extension Velocities in Level Set Methods,” *J. Comput. Phys.*, 1999.
- [105] G. Caselles, Vicent and Kimmel, Ron and Sapiro, “Geodesic active contours,” *Int. J. Comput. Vis.*, vol. 22, no. 1, pp. 61–79, 1997.
- [106] F. Meyer, “Topographic distance and watershed lines,” *Signal Processing*, vol. 38, no. 1, pp. 113–125, 1994.
- [107] S. Dimopoulos, C. E. Mayer, F. Rudolf, and J. Stelling, “Accurate cell segmentation in microscopy images using membrane patterns,” *Bioinformatics*, vol. 30, no. 18, pp. 2644–2651, 2014.
- [108] J. Klein, S. Leupold, I. Biegler, R. Biedendieck, R. Münch, and D. Jahn, “TLM-tracker: Software for cell segmentation, tracking and lineage analysis in time-lapse microscopy movies,” *Bioinformatics*, vol. 28, no. 17, pp. 2276–2277, 2012.
- [109] K. Zhang, L. Zhang, H. Song, and W. Zhou, “Active Contours with Selective Local or Global Segmentation: A New Formulation and Level Set Method,” *Image Vis. Comput.*, vol. 28, no. 4, pp. 668–676, 2010.
- [110] N. Otsu, “A threshold selection method from gray-level histograms,” *IEEE Trans. Syst. Man. Cybern.*, vol. 9, no. 1, pp. 62–66, 1979.
- [111] L. Lam, S.-W. Lee, and C. Y. Suen, “Thinning methodologies - a comprehensive survey,” *IEEE Trans. Pattern Anal. Mach. Intell.*, vol. 14, no. 9, pp. 869–885, 1992.
- [112] J. Zakrisson, K. Wiklund, O. Axner, and M. Andersson, “Tethered cells in fluid flows—beyond the Stokes’ drag force approach,” *Phys. Biol.*, vol. 12, no. 5, p. 056006, 2015.
- [113] M. Andersson, “Construction of force measuring optical tweezers instrumentation and investigations of biophysical properties of bacterial adhesion organelles,” Umeå University, Umeå, 2007.
- [114] G. Lamour, J. B. Kirkegaard, H. Li, T. P. J. Knowles, and J. Gsponer, “Easyworm: An open-source software tool to determine the mechanical properties of worm-like chains,” *Source Code Biol. Med.*, vol. 9, no. 1, pp. 1–6, 2014.
- [115] D. Boal, *Mechanics of the cell, second edition*. 2012.
- [116] J. Happel and H. Brenner, *Low Reynolds Number Hydrodynamics*. 1983.
- [117] N. P. Boks, W. Norde, H. C. van der Mei, and H. J. Busscher, “Forces involved in bacterial adhesion to hydrophilic and hydrophobic surfaces,” *Microbiology*, vol. 154, no. 10, pp. 3122–3133, 2008.
- [118] E. Loth, “Drag of non-spherical solid particles of regular and irregular shape,” *Powder Technol.*, vol. 182, no. 3, pp. 342–353, 2008.
- [119] A. Krizhevsky, I. Sutskever, and G. E. Hinton, “Alexnet,” *Adv. Neural Inf. Process. Syst.*, 2012.